Insights into the Transport and Fragmentation Characteristics of Earthquake-Induced Rock Avalanche: Numerical Study

Ge Gao[1]; Mohamed A. Meguid, Ph.D., M.ASCE[2]; Luc E. Chouinard, Sc.D.[3]; and Chong Xu, Ph.D.[4]

Abstract: The earthquake-induced rock avalanche in the Tangjia Valley was the most notable geological disaster triggered by the Lushan earthquake in 2013. In order to investigate the transport kinematics and depositional mechanism of this catastrophic landslide, a 2D discrete element model was developed and calibrated using field data. The model was then used to analyze the seismic response and mass transport process of a natural slope. The slope response to earthquake was numerically studied focusing on crack initiation, propagation, and coalescence within the rock mass. The mass movement and accumulation process were interpreted in terms of evolution of stress and solid fraction, kinematic behavior, and energy conversion. During the mass transport process, the slope was fragmented progressively due to intense shearing, allowing a basal layer of gradually fining solid particles to be generated with simultaneous occurrence of violent collisions, increase in particle kinematic activities, and the reduction of solid concentration. To further study this deformation process, fragment size distributions and fractal dimensions were described by Weibull distribution and power-law function, respectively. This statistical analysis reveals that dynamic disintegration continuously operates with the increasing runout distance. It is also found that the distribution of the fragment shapes becomes stable as the avalanche loses its momentum and deposition starts in the runout area. The proposed framework for the analysis of rock avalanches can be used to understand the physics of similar geological hazards. **DOI: 10.1061/(ASCE)GM.1943-5622.0001800**.

Author keywords: Earthquake-induced landslide; Rock avalanche; Fragmentation; Fragment shape; Discrete element analysis.

Introduction

Large earthquakes in mountainous regions commonly result in catastrophic and widespread landsliding, which is a significant hazard during and in the immediate aftermath of ground shaking (Keefer 1994). These events have been reported worldwide in the past few decades. For example, coseismic landslides that developed during the 2005 Kashmir earthquake ($Ms = 7.6$) caused about 30% of the total fatalities (Havenith and Bourdeau 2010). In the 2008 Wenchuan earthquake ($Ms = 8.0$), a quarter of the total deaths and over one-third of the total damage costs were caused by earthquake-triggered landslides (Yin et al. 2009). Less than five years later, a strong shock happened once again along the Longmen Shan fault zone located about 80 km southwest of the epicenter of the 2008 event and induced as many as 15,645 coseismic landslides (Xu et al. 2015a, b). In recent years, there has been an increasing interest in the study of earthquake-triggered landslides; however, much uncertainty still exists regarding the transport mechanism and fragmentation process.

Rock avalanches are among the most destructive landslides that are commonly triggered by strong earthquakes. In the literature, many hypotheses have been proposed to explain the rock transport kinematics and dynamics, including air or vapor lubrication (Kent 1966; Shreve 1968; Habib 1975), mechanical fluidization (Bagnold 1954; Davies 1982), momentum transfer (Eisbacher 1979; Davies et al. 1999), acoustic fluidization (Melosh 1986), energetic disintegration (Davies and McSaveney 1999), and basal rock melting (Erismann and Abele 2001; De Blasio and Elverhøi 2008). Although some of the invoked mechanisms may be important for some specific events, none has so far gained universal acceptance for elucidating the rock avalanche mobility. In natural conditions, the deposited material in long-runout rock avalanches has been observed in diverse geological conditions to be composed of highly fragmented parent material (Locat et al. 2006; Crosta et al. 2007; Perinotto et al. 2015; Wang et al. 2015; Zhang et al. 2019). Thus, dynamic rock fragmentation within the flow has been invoked as a possible mechanism for effective lubrication in rock avalanches (Davies et al. 1999; Davies and McSaveney 2009; McSaveney and Davies 2009). The related research has been performed by means of field observations of real rock avalanche deposits (Locat et al. 2006; Crosta et al. 2007; Dunning et al. 2007; Zhang and Yin 2013) and laboratory experiments (Giacomini et al. 2009; Imre et al. 2010; Bowman et al. 2012; Haug et al. 2016). Crosta et al. (2007) described the spatial distributions of the fractal dimension values measured at both the source and the deposit areas, which delineate the fragmentation process and the corresponding energy consumption. Imre et al. (2010) performed a series of centrifuge tests and stated that the interparticle collisions play a dominant role in the fragmentation of a rock avalanche.

Extensive effort has been exerted to reproduce the runout behavior of landslides numerically (Campbell 1990; Calvetti et al. 2000; Campbell 2006; Antolini et al. 2016; Gong and Tang 2017;

[1]Graduate Student, Civil Engineering and Applied Mechanics, McGill Univ., 817 Sherbrooke St. W., Montreal, QC H3A 0C3. ORCID: https://orcid.org/0000-0001-5405-5590. Email: ge.gao2@mail.mcgill.ca

[2]Professor, Civil Engineering and Applied Mechanics, McGill Univ., 817 Sherbrooke St. W., Montreal, QC H2A 0C3 (corresponding author). ORCID: https://orcid.org/0000-0002-5559-194X. Email: mohamed.meguid@mcgill.ca

[3]Associate Professor, Civil Engineering and Applied Mechanics, McGill Univ., 817 Sherbrooke St. W., Montreal, QC H2A 0C3. Email: luc.chouinard@mcgill.ca

[4]Researcher, Institute of Crustal Dynamics, China Earthquake Administration, Beijing 100085, China. ORCID: https://orcid.org/0000-0002-3956-4925. Email: xuchong@ies.ac.cn

Note. This manuscript was submitted on October 1, 2019; approved on April 28, 2020; published online on July 8, 2020. Discussion period open until December 8, 2020; separate discussions must be submitted for individual papers. This paper is part of the ***International Journal of Geomechanics***, © ASCE, ISSN 1532-3641.

Shen et al. 2017, 2018; Gao and Meguid 2018a, b), particularly as the complex nature and rapid process of landslides may not be comprehensively analyzed using field investigations or experiments. Such efforts involve the application of discrete or continuum methods. The continuum method is inherently capable of simulating the dynamic movements of actual landslides. However, continuum-based numerical models often fail to reproduce the progressive failure of rock slopes, especially the dynamic release and the accompanying complex internal distortion, dilation, and fracture (Stead et al. 2006). Unlike continuum models, the discrete element method (DEM), does not limit the extent of element separation, and the mass movement process from fracture to separation can be fully simulated. More importantly, from the mesoscopic view, the internal disruption of rock avalanches very high signifies the nearly complete disaggregation into individual soil grains or small rock fragments. Therefore, the DEM is considered an effective tool for modeling rock avalanches, in which the avalanching process is extremely rapid and exceedingly complex involving sliding or flow. By employing DEM simulations, Campbell (1989) demonstrated that particles in the base exhibit high fluctuations with increase of granular temperature and thus increasing apparent friction reduction of landslides. Campbell et al. (1995) observed that the stratification is well preserved in their original order within the debris and suggested that the material at the top of the debris may have been very gently handled, which accounts for the large, angular, and obviously unagitated fragments found on the surface of the actual landslide deposit.

A large body of literature on DEM aspects of modeling earthquake-induced landslides focused on the kinematic behavior and deformation evolution of the actual landslides triggered by seismic activities only throughout simple recording of the displacements and velocities (e.g., Tang et al. 2009; Zhou et al. 2013; Yuan et al. 2014). However, less attention has been paid to studying the dynamic fragmentation process and transport mechanism of earthquake-induced landslides with complex geological and geomorphological settings (Meunier et al. 2007; Zhao and Crosta 2018). Therefore, the Tangjia Valley rock avalanche, as one of the few identified large-scale landslides resulting from the seismic event of the Lushan earthquake, is selected as a natural laboratory to investigate the characteristics of earthquake-induced rock avalanche, including joint distribution, crack evolution, energy transition, dynamic fragmentation, and deposition pattern. In this study, a suitable set of microparameters was calibrated using uniaxial compression strength (UCS), and the developed numerical model is validated based on the recorded information at the site. The sedimentary fabric within the rock deposit and the fragment statistics presented in this study provide new insight into the deposition mechanism of a bonded granular system associated with a large-scale rock avalanche.

Tangjia Valley Rock Avalanche

The Tangjia Valley rock avalanche (30° 10′ 43″ N, 102° 45′ 40″ E) occurred in the Damiao village, Laochang Township, Tianquan county, Sichuan province, China, and is the largest rock avalanche triggered by the Lushan earthquake.

Geological and Geomorphologic Setting

The 2013 Lushan earthquake occurred on the easternmost margin of the Tibetan plateau. A series of predominantly north-northeast striking thrust faults were observed at the base of the Longmen Shan Mountains, at the northwestern edge of the Sichuan Basin (Tang et al. 2015). The fault belt consists of three thrust faults: the Maoxian-Wenchuan fault (back-range fault), the Yingxiu-Beichuan fault (central fault), and the Guanxian-Jiangyou fault (front-range fault). The 2008 Wenchuan earthquake occurred on the central part of the Longmen Shan fault belt, whereas the 2013 Lushan earthquake occurred on the southwestern segment. The epicenter of the Lushan event was near the Shuangshi-Dachuan fault [see Fig. 1(a)]. The Tangjia Valley rock avalanche is located in the footwall of the fault branch [see Fig. 1(b)]. The violent ground shaking triggered by the seismic fault resulted in the largest Lushan earthquake-triggered landslide. In the rock avalanche area [Fig. 1(b)], lithology of the footwall (southeast plate) is composed of late Triassic light gray thick sandstone, quartzitic sandstone, mudstone of Xujiajointe Group (T_3x), and the Quaternary deposits (Q_d^{del}) with a thickness of 3–5 m. The hanging wall (northwest plate) is composed of early Triassic purple silty mudstone and dolomitic sandstone in moderate-thin layers (T_1f) and thick, gray dolomitic limestone of Jialingjiang Group (T_1j), which is overlapped by the Leikoupo Group (T_2l) of the middle Triassic age.

From a geomorphologic point of view (Fig. 2), rock avalanche source area lies on a narrow mountain ridge with an average width of 10 m, which is characterized by two steep lateral flanks with slope gradients of 60°–63°, and deeply incised valleys (i.e., Chunjianwo and Gangoutou valleys) in the frontal region.

Failure Mechanism and Dynamic Process

The landslide can be divided into the following four areas: the source area, transport area, deposition area, and converging area (see Fig. 3), and the corresponding possible failure process is as follows (Hu et al. 2013; Li et al. 2017):

1. The intense seismic shakings loosened and weakened the slope materials, facilitating further degradation of highly weathered rock mass strength. As a result, the rock slopes shattered and collapsed at a high speed, afterward the rock material traveled toward the direction of 130° over a short time period from the source area. At an elevation of 1,500 m a.s.l., due to the presence of the mountain ridge [see Fig. 4(a)], the displaced slope mass was split into two streams [see Fig. 3(a)], that is, the left stream (rock avalanche I) toward the direction of 104° and the right stream (rock avalanche II) toward the direction of 156°. Thus, the source area can be divided into two subzones: S-Ia and S-Ib, which represent the source area for the left stream [Figs. 3(b) and 4(b)] and right stream [Figs. 3(c) and 4(c)], respectively. The complete geometric and geologic information of the source area is summarized in Table 1.
2. The slope mass ran down rapidly in the transport areas T-IIa and T-IIb for the left and right stream, respectively. Subsequently, the translating slope mass was transformed into debris flows as it collided onto the opposite mountains of the left bank of Chunjianwo Valley and the right bank of Gangoutou Valley for the left and right streams, respectively. After the rock mass disintegrated, a small portion of the material within the left stream climbed up against the opposite valley bank to a maximum height of 35 m at location A1 [see Fig. 3(a)], whereas most of the fragmented rock continued traveling rapidly along the steep terrain. In addition, the sliding mass of the right stream super-elevated on the right bank of the Gangoutou Valley with a height of 15 m at location B1 [see Fig. 3(a)], which forced the fragmented rock flow to move with a 33° deflection and then continued to travel downward in a rapid motion along the valley.

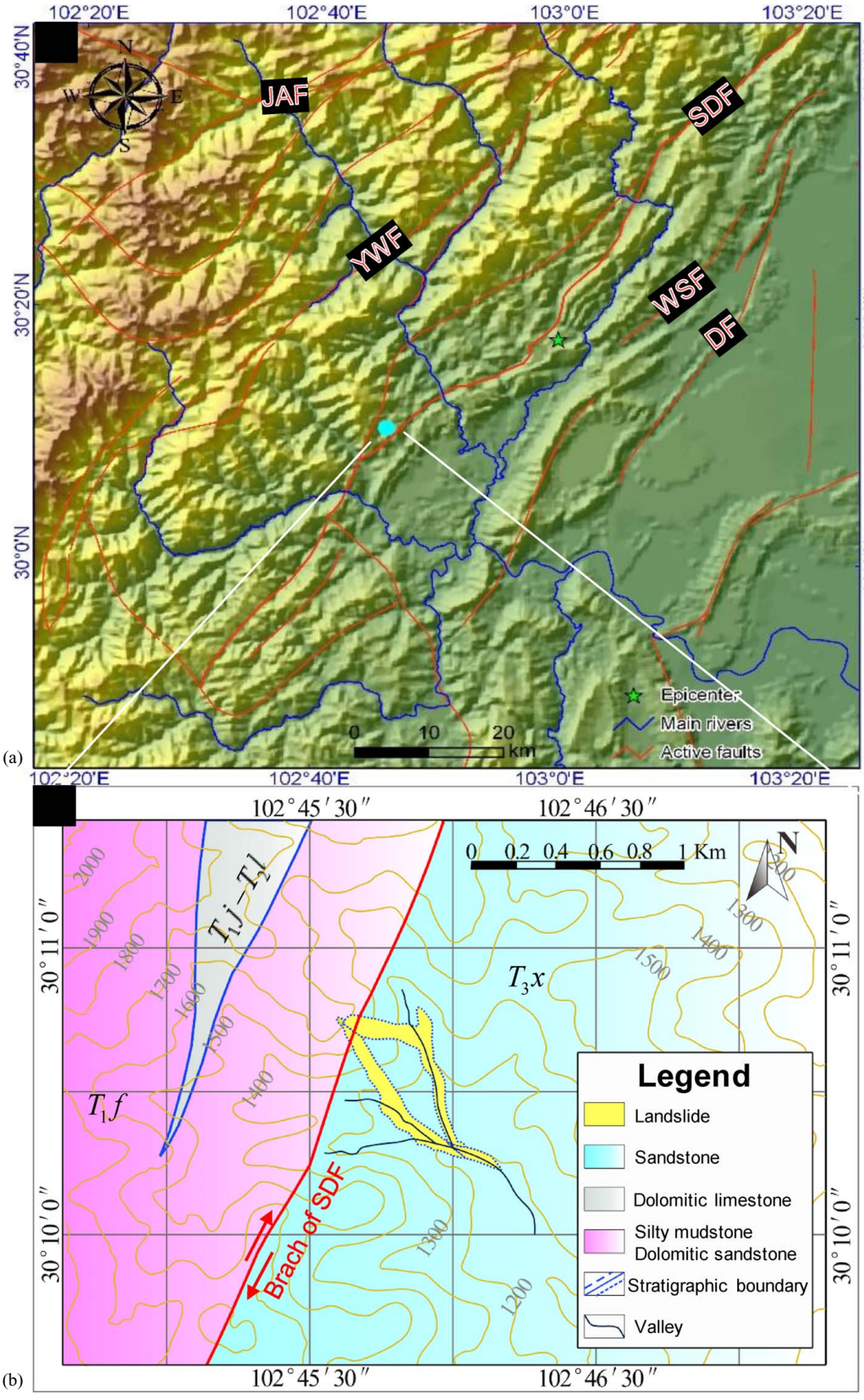

Fig. 1. (a) The tectonic setting of the 2013 Lushan earthquake (SDF = Shuangshi-Dachuan fault; WSF = Western Shangli fault; DF = Dayi fault; YWF = Yanjing-Wulong fault; and JAF = Jintang Arc fault); and (b) a geological map of landslide area. (Adapted from Xu et al. 2015a.)

3. Due to the longitudinal gradients of the valleys being relatively small with 17.5‰ (≈10°) for Chuanjiawo Valley and 144‰ (≈8°) for Gangoutou Valley, respectively. The left stream debris accumulated in the subzone D-IIIa, which was located along the Chunjianwo Valley at elevations ranging from 1,170 to 1,270 m a.s.l. [Figs. 3(a) and 4(d)]. The right stream debris accumulated in the subzone D-IIIb, which was located along the Gangoutou Valley at elevations ranging from 1,170 to 1,215 m a.s.l.

Fig. 2. Overview of local geomorphologic conditions of the Tangjia Valley rock avalanche. (Image: Google Earth, CNES/Airbus, 2019)

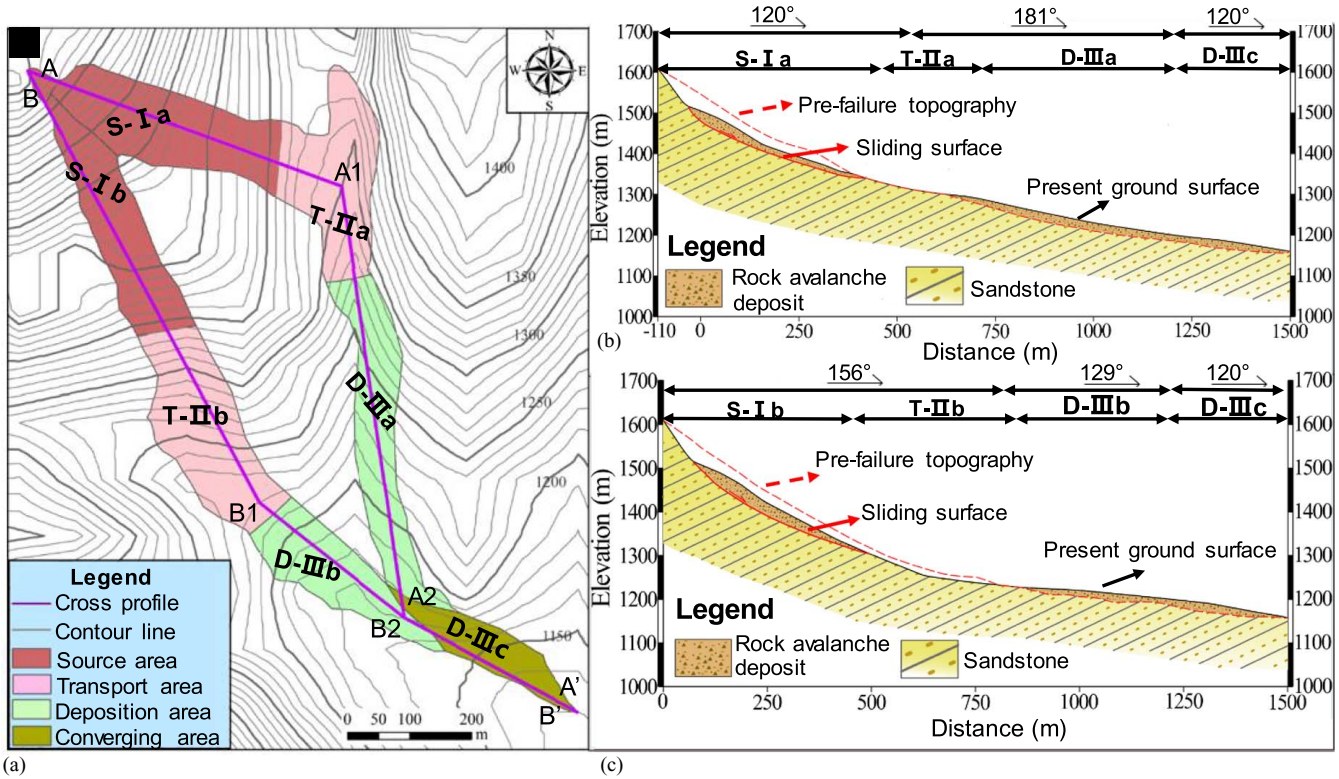

Fig. 3. (a) Detailed topography of the Tangjia Valley rock avalanche along the main movement direction; (b) geological section map of the left stream of the avalanche along line A–A′; and (c) geological sectiGoogle on map of the right stream of the avalanche along line B–B′.

4. After running out a distance of around 763 and 409 m for left and right stream, respectively, the displaced material converged in the area D-IIIc [see Figs. 3(a) and 4(e)] at an elevation ranging from 1,144 to 1,170 m a.s.l. Finally, with the decrease of mass movement velocity, the landslide came to a halt at the Tangjia Valley after traveling about 223 m.

Discrete Element Modeling

Numerical Model

In this distinct element (DE) analysis, the rock mass is simulated as an assembly of particles cemented together using the parallel-bond

Fig. 4. Characteristics of the Tangjia Valley rock avalanche: (a) the mountain ridge controls the landslide initiation; (b) the upper part of the Chunjianwo Valley toward the source area; (c) the upper part of the Gangoutou Valley toward the source area; (d) deposits in the Chunjianwo Valley; and (e) the two streams converge into the Tangjia Valley.

Table 1. Field information of source area

Geometric and geologic conditions	Zone S-Ia	Zone S-Ib
Length (m)	160–170	230–240
Width (m)	110	75
Average slope (°)	53	50
The head scarp in elevation (m)	1,605	1,600
The toe of rupture surface in elevation (m)	1,340	1,340
Height difference (m)	265	260

model (Itasca Consulting Group 2014). The parallel-bond models, characterized by tensile and shear strength and normal and tangential stiffness, have been widely used to study cracking and fragmentation of rock material (Potyondy and Cundall 2004).

The maximum tensile and shear stresses acting on the parallel-bond periphery are calculated from the beam theory to determine whether an interparticle bond breaks, as

$$\bar{\sigma} = \frac{\bar{F}_n}{\bar{A}} + \frac{\|\bar{M}_b\|\bar{R}}{\bar{I}} \tag{1}$$

$$\bar{\tau} = \frac{\|\bar{\mathbf{F}}_\mathbf{s}\|}{\bar{A}} + \begin{cases} \dfrac{|\bar{M}_t|\bar{R}}{\bar{J}}, & \text{3D} \\ 0, & \text{2D} \end{cases} \tag{2}$$

where $\bar{F}_n$, $\bar{\mathbf{F}}_\mathbf{s}$ = normal and shear parallel-bond force; $\bar{M}_t$, $\bar{\mathbf{M}}_\mathbf{b}$ = twisting and bending parallel-bond moments; $\bar{R}$, $\bar{A}$, $\bar{I}$, and $\bar{J}$ = the bond radius of the cross-sectional area, moment of inertia

of the parallel-bond cross-section, and the polar moment of inertia of the parallel-bond cross-section, respectively.

Fig. 5 shows the numerical model of the rock avalanche, built using PFC^{2D} 5.0 based on the profile map depicted in Figs. 3(b and c). The sliding surface is modeled using wall elements and the sliding body is constructed using 12,000 and 12,056 ball elements with the same particle size distribution for the left and right streams of the avalanche, respectively [Figs. 5(a and b)]. On the basis of *in situ* observation in the landslide area (Hu et al. 2013), the adopted minimum disk diameter is 1.0 m and the size ratio r_{max}/r_{min} of the rigid particles is taken as 1.66 to prevent a reorganization of the particles within a closed-packed lattice, which otherwise would dramatically alter the behavior of the particle assembly (Potyondy and Cundall 2004; Imre et al. 2010). To gain insights into the kinematics and dynamics of the left stream of the avalanche, four particles were monitored, as shown in Fig. 5(a). In addition, to better visualize the emplacement process of the landslide, six layers were identified using different colors (see Fig. 5). It is worth noting that only the left stream of the avalanche was analyzed thoroughly in this study to illustrate the mechanism of the earthquake-induced landslides. The right stream of the rock avalanche is presented, however, for the purpose of comparison and validation.

Physical and Mechanical Parameters

To enable the use of PFC models as a reliable simulation tool, it is necessary to establish a reasonable relationship between the numerical parameters and the mechanical characteristics of the problems (Potyondy and Cundall 2004). However, there is no straightforward relationship between macroscopic and microscopic parameters (Calvetti et al. 2000; Tang et al. 2009; Garcia and Bray 2018; Gao and Meguid 2018c). In this study, the microparameters needed for the PFC model (Table 2) are derived from uniaxial compression (Fig. 6). The unconfined compressive strength of the rock

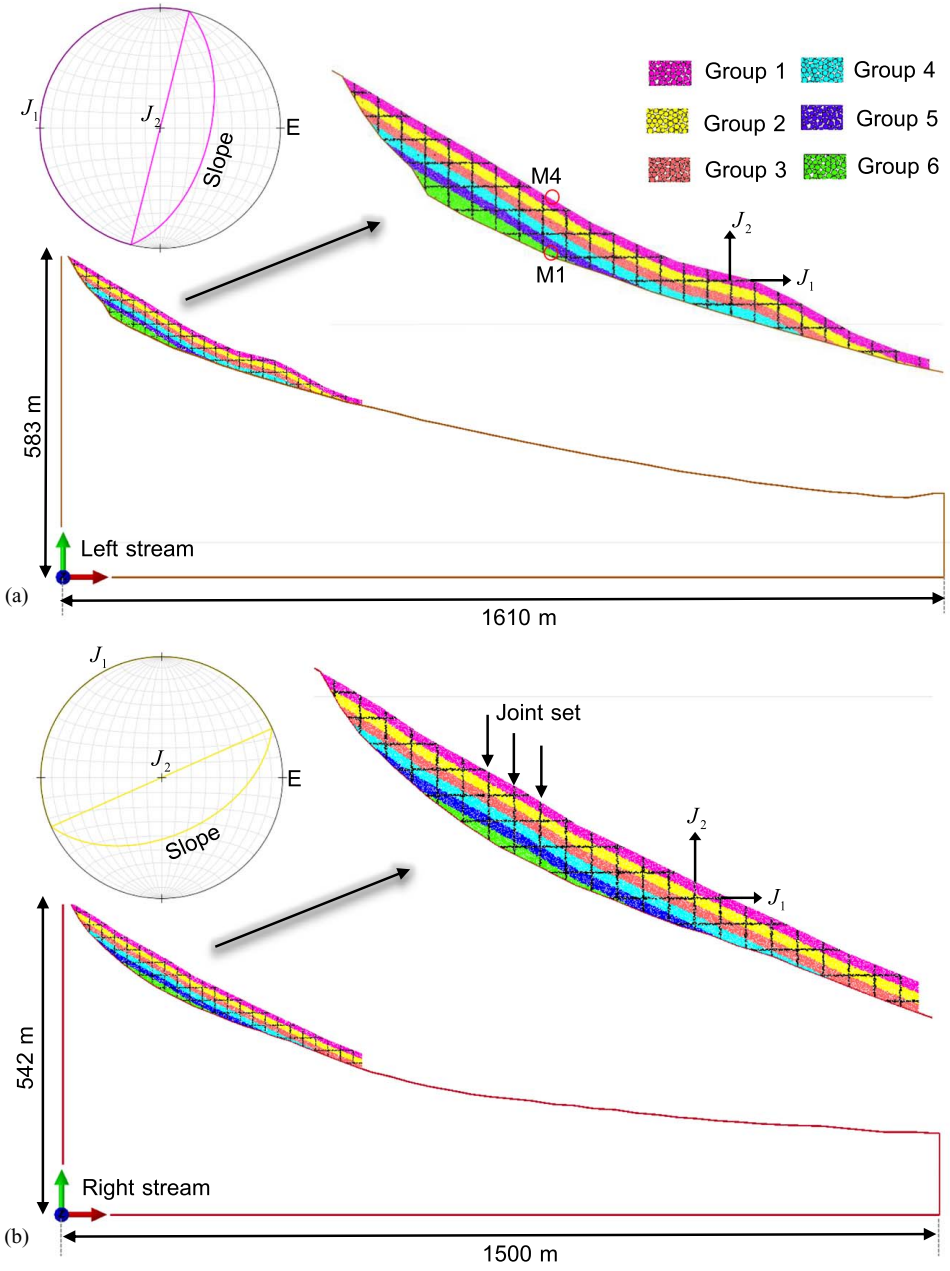

Fig. 5. Two-dimensional discrete element model of the rock avalanche: (a) left stream; and (b) right stream.

mass (UCS_m) and Poisson ratio (ν) are fitted with that of Tangjia Valley rock mass. The UCS_m of the Tangjia Valley rock mass (mainly sandstone) is estimated to be 3.45 MPa, by an empirical relationship $UCS_m = \sqrt{S}UCS_r$ (Hoek and Brown 1997; Hoek et al. 2000), where UCS_r, the unconfined compressive strength of intact sandstone, is 108.9 MPa, according to Chang and Zhang (2007); S is an empirical parameter related to discontinuities in the rock mass that is estimated to be 0.001 according to Hoek et al. (2000).

Earthquake Loading and Boundary Conditions

After the primary stress field is generated due to gravity, seismic motion is applied at the wall boundary by integrating the corrected accelerations recorded at the Baoxing seismic station during the Lushan earthquake. Seismic shaking duration of 45 s is adopted in this study. Fig. 7 shows the combined acceleration records used in the analysis. Velocity time histories [Figs. 7(b, d, and f)] are obtained by integrating the acceleration records [Figs. 7(a, c, and e)], respectively. The horizontal earthquake waves represent the projection in the main sliding directions (N104°E) and (N156°E) for the left and right streams of the avalanches using the acceleration records in E–W and N–S directions as computed by Eqs. (3) and (4), respectively. The input vertical earthquake velocity [Fig. 7(f)] is integrated from the acceleration records in U–D direction, as shown in Fig. 7(e).

$$a_H^{\text{Left}} = a_{\text{E-W}} \cdot \sin 104^\circ + a_{\text{N-S}} \cdot \cos 104^\circ \quad (3)$$

Table 2. Micromechanical parameters used for the DE model

Parameter	Assigned value
Particle density	2,600
Friction coefficient (ball-ball)	0.4
Friction coefficient (ball-wall)	0.15
Effective contact modulus (GPa)	5
Normal-to-shear stiffness ratio (kn/ks)	2.5
Bond effective modulus (GPa)	6
Bond normal-to-shear stiffness ratio ($\bar{k}n/\bar{k}s$)	2.5
Parallel-bond tensile strength (MPa)	3.44
Parallel-bond cohesion (MPa)	3.44
Parallel-bond friction angle (Degree)	30
Parallel-radius multiplier (–)	1.0

$$a_H^{\text{Right}} = a_{\text{E-W}} \cdot \sin 156^\circ + a_{\text{N-S}} \cdot \cos 156^\circ \quad (4)$$

where a_H^{Left} and a_H^{Right} = the horizontal accelerations of the left and right streams, respectively; $a_{\text{N-W}}$ and $a_{\text{N-S}}$ = the acceleration records in the east-west and north-south directions, respectively. The angles 104° and 156° represent the main sliding directions for the left and right streams of the avalanches, respectively.

Joint Characteristics

In addition to the discontinuities that are normally considered in estimating rock mass strength, larger discontinuities, such as bedding surfaces and joints, cannot be disregarded when constructing a numerical model (Barla et al. 2011; Zou et al. 2017). In particular, the Tangjia Valley rock slope is heavily jointed according to field investigations. Many of the rock blocks found in the rock avalanche are broken along pre-existing discontinuities, such as bedding surfaces and joint sets. However, it is not practical to reconstruct the exact system of joint sets due to the complicated nature of the discontinuities and unfavorable site conditions at the source area. Therefore, debonding particles along the orthogonal planes (J_1 and J_2) with an average spacing of 20 m are incorporated in the 2D DE model (see Fig. 5) to approximately simulate the natural joint systems at the site. In addition, it is worth noting that all joints are assumed to be fully persistent along the orthogonal pattern, so that they can slice the rock block completely.

Damping

Previous studies reported by Calvetti et al. (2000), Zhou et al. (2016), Gao and Meguid (2018a, b), and Zhang and Evans (2019) illustrated that dynamic simulations are sensitive to the presence of damping. Moreover, in a system of particles, energy is mainly dissipated through frictional sliding and viscous damping at particle–particle or particle–wall contacts (Zou et al. 2017). Viscous damping, proportional to the relative velocities of the particles in contact, is employed to replicate the energy dissipated by particle asperities being sheared off and the plastic deformations of the contacting particles. In this study, the viscous normal v_n and shear v_s damping constants of granular particles within the rock mass (particle–particle contacts) are selected to be $v_n = v_s = 0.02$, which are similar to those adopted by Zhao et al. (2017). As stated by

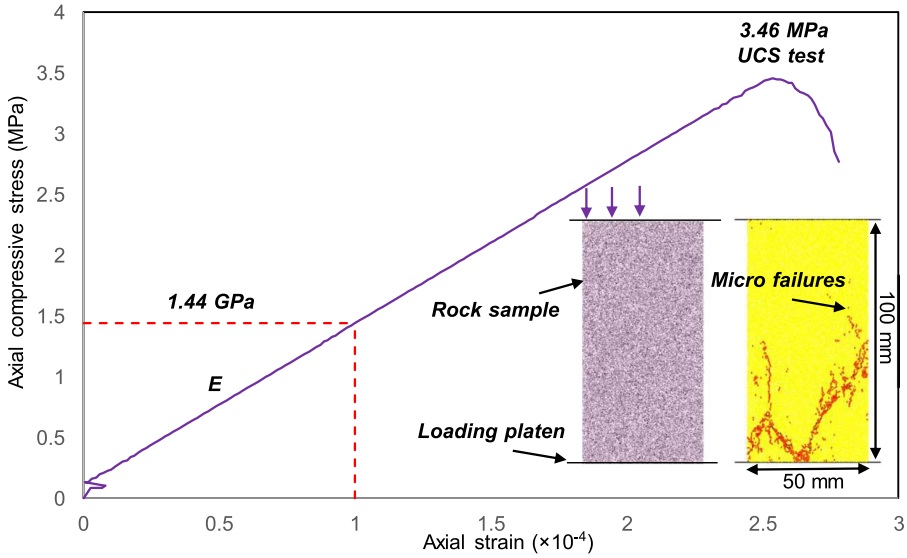

Fig. 6. Modeling the unconfined compression test.

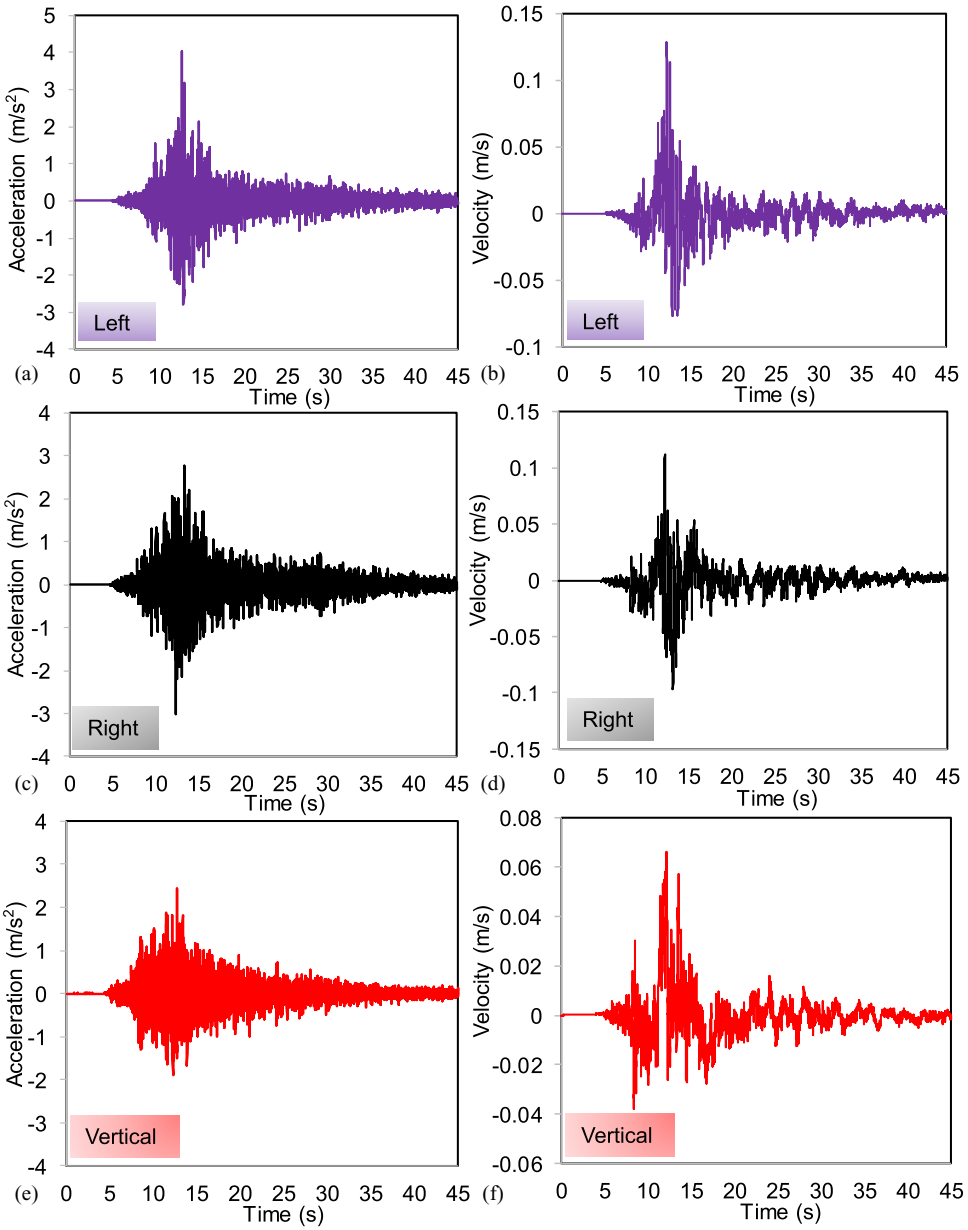

Fig. 7. Seismic time history curves: (a) horizontal acceleration for the left stream; (b) horizontal velocity for the left stream; (c) horizontal acceleration for the right stream; (d) horizontal velocity for the right stream; (e) vertical acceleration; and (f) vertical velocity.

McNamara (2013), the high viscous damping at the base could effectively mimic the absorbing boundary condition for the seismic wave transmission and reflection at the slope base, therefore, the normal and shear damping coefficients of the particles along the failure plane (particle–wall contacts) are selected to be 0.21 and 0.02, respectively, as suggested by Feng et al. (2017).

Simulation Results

Kinematics of the Rock Avalanche

Fig. 8(a) shows that the rock avalanche experiences a complex sequence of accelerations and decelerations as the earthquake wave propagates. The average velocity reaches 10 m/s after approximately 15 s, and attains a peak value of 15 m/s at $t = 30$ s. At that time, most of the avalanche material disintegrates and departs from the cliff, as shown in Figs. 9(a and b). Afterward, the rock avalanche gradually decelerates to 10 m/s at $t = 45$ s, and the subsequent landslide deposition leads to continuous decrease of velocity until it finally become 0 at $t = 75$ s. The comparison between the rock avalanche at $t = 45$ s [Fig. 9(c)] and the final deposit in Fig. 9(d) illustrates that the rock avalanche completes most of its long-runout motion during earthquake excitement, which accords well with the field observations (Hu et al. 2013). Therefore, the movement process can be divided into three phases: (1) early acceleration ($t < 10$ s) with low seismic shaking intensity; (2) high-speed long-runout with intense seismic shakings (10 s $< t <$ 45 s); (3) final, low-speed deposition under gravity only ($t > 45$ s). The maximum velocities of the rock mass are then used to reveal the agitation in the rock avalanche. The maximum velocities can be found such that $V_{max} = \max(v_i)$, where v_i is the velocity of a granular particle at a certain time, and i ranges from 1 to n; n is the number of the particles in the DE model. It is shown that the maximum velocity of the granular system is between 40 and 45 m/s, which is approximately three times higher than the average velocity of the avalanche mass.

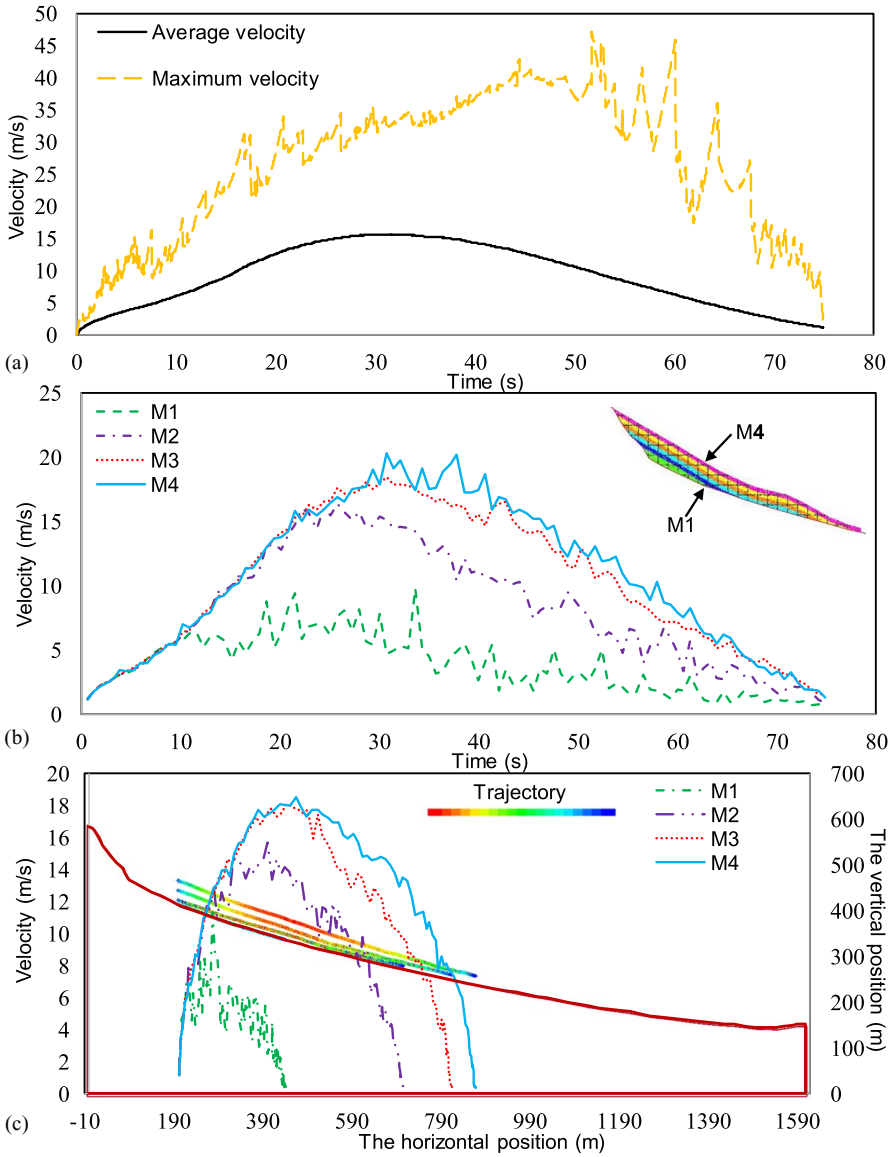

Fig. 8. (a) Maximum and average velocities of the mass during motion; (b) velocities of the monitoring points along a vertical section with the time; and (c) velocity trajectories of the monitoring particles along a vertical section.

The average velocity of the rock avalanche gradually declines after $t = 30$ s, while the maximum velocity of the flowing mass remains high up to $t = 60$ s. This observation indicates that despite the fact that the partial deposition with a decrease in seismic shaking intensity results in a drop in the average velocity, some of the far-traveled particles continue to travel at high speed under gravity accompanied by the ongoing disintegration and fragmentation processes. The analyses of both the average and the maximum velocity of the granular system can be used as a complementary way to quantify the intensity of the rock mass movement in the perspective of time and location.

Fig. 8(b) shows that particles originating at a given vertical section of the avalanche body have similar velocity trends, indicating that they follow similar acceleration and deceleration patterns; however, the velocities decrease gradually from the top to the bottom of the slide. During the first 10 s, the velocities of the monitored particles are almost the same, which indicates that the avalanche mass is moving as one unit. The velocities then increase at a distinct rate, with maximum velocities appearing at 20–40 s. Subsequently, the speeds gradually decrease, with the avalanche gradually starting to deposit after the end of the seismic loading at a time of 45 s. Though rock blocks from the upper layers of the avalanche experience more runout distance and higher velocities than those that originated in the lower layer, the trajectories of the monitoring points show that their relative vertical positions are maintained during the landslide propagation and deposition [see Fig. 8(c)], indicating strata are well preserved in their original order within the debris. This can be verified by the granular dynamic evolution, shown in Figs. 9(a–d), in which the colored layers are preserved in their original order. This phenomenon of stratigraphy preservation has also been reported in some well-documented numerical and field investigations (Campbell et al. 1995; Chang and Taboada 2009; Thompson et al. 2009; Zhao and Crosta 2018).

The evolving motion of the rock avalanche is presented in Figs. 9(a–d). At the early stage [Fig. 9(a)], the seismic velocities in the two directions reach their peak values. Meanwhile, failure starts at several closely spaced points and multiple cracks grow simultaneously relaxing the tensile stresses within the tail region of the avalanche due to the downward pulling forces exerted by the lower avalanche mass. Between 12.6 and 30 s, the intense shakings result in high shear stresses at the base. Consequently,

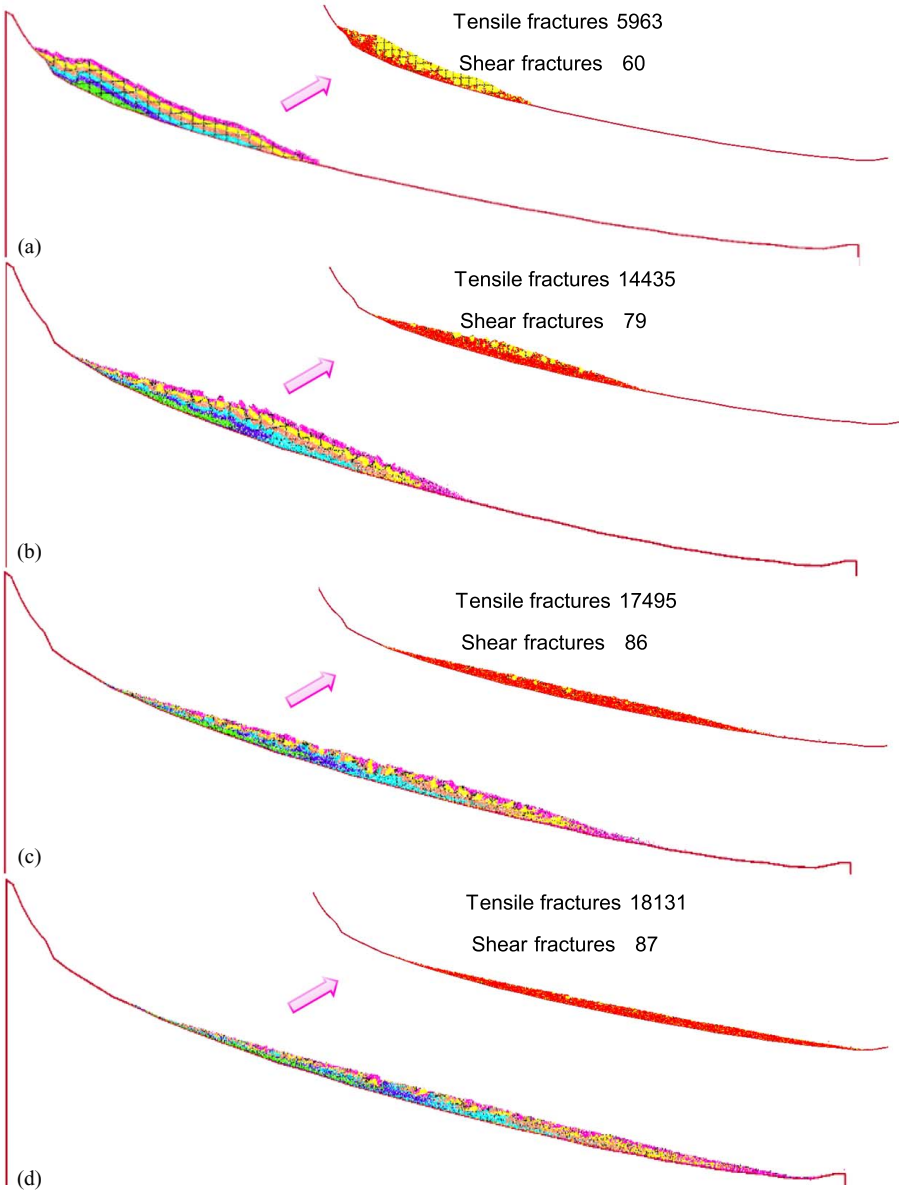

Fig. 9. Evolution of the landslide process at different time stamps: (a) $t = 12.6$ s; (b) $t = 30$ s; (c) $t = 45$ s; and (d) $t = 75$ s.

cracks develop and grow to coalescence from both the front and tail regions toward the middle of the moving rocks [Fig. 9(b)]. This facilitates fragmentation and pulverization of the solid rocks within the middle region. The entire avalanche body, then, accelerates and runs down the valley [Fig. 9(c)]. Finally, the rock avalanche decelerates and settles gradually [Fig. 9(d)]. The displaced material travels a horizontal runout distance of about 1,560 m with a descent of approximately 447 m. This corresponds to a Fahrböschung of 16°, which is slightly smaller than the 16.7° reported by Li et al. (2017).

Stress Evolution and Solid Concentration

In order to gain further insights into the dynamic process of rock mass movement, the stress and the solid fraction fields inside the avalanche were computed using the spatial interpolation techniques, which has been applied by Mollon et al. (2012) to analyze the collective behavior of granular flows in a planar slope. The average stress evolution, as demonstrated in Fig. 10(a) correlates well with the progression of the fracturing. The stress concentration begins at the basal region of the granular mass. The increase of these stresses may facilitate the fracture and block fragmentation of the slope mass. The cracks are initiated at the joint tips, propagated, and cut through the rock bridges. The coalescence of cracks in the basal region [see Fig. 9(b)] results in higher stresses [see Fig. 10(a)], promoting the development of fragmented fine-grained basal shearing layers during avalanche emplacement. As the cracks propagate to the surface, then cluster and coalesce in the main body with the avalanche transiting into the deposition phase, the major part of the avalanche body will be severely disintegrated as shown in Figs. 9(b and c) and only some coarse-grained blocks will be embedded in a fine-grained matrix. In addition, it is worth noting the low stresses at the top of the slope help to preserve the angular surface or fractured coarse blocks, often found in large avalanche deposits.

As stated by Mollon et al. (2012), the solid fraction can provide a good qualitative assessment of the kinematics and dynamics inside the flow. First, a representative volume is defined for the particles in the area that needs to be investigated. This representative volume is defined by the nonconvex envelope of neighboring

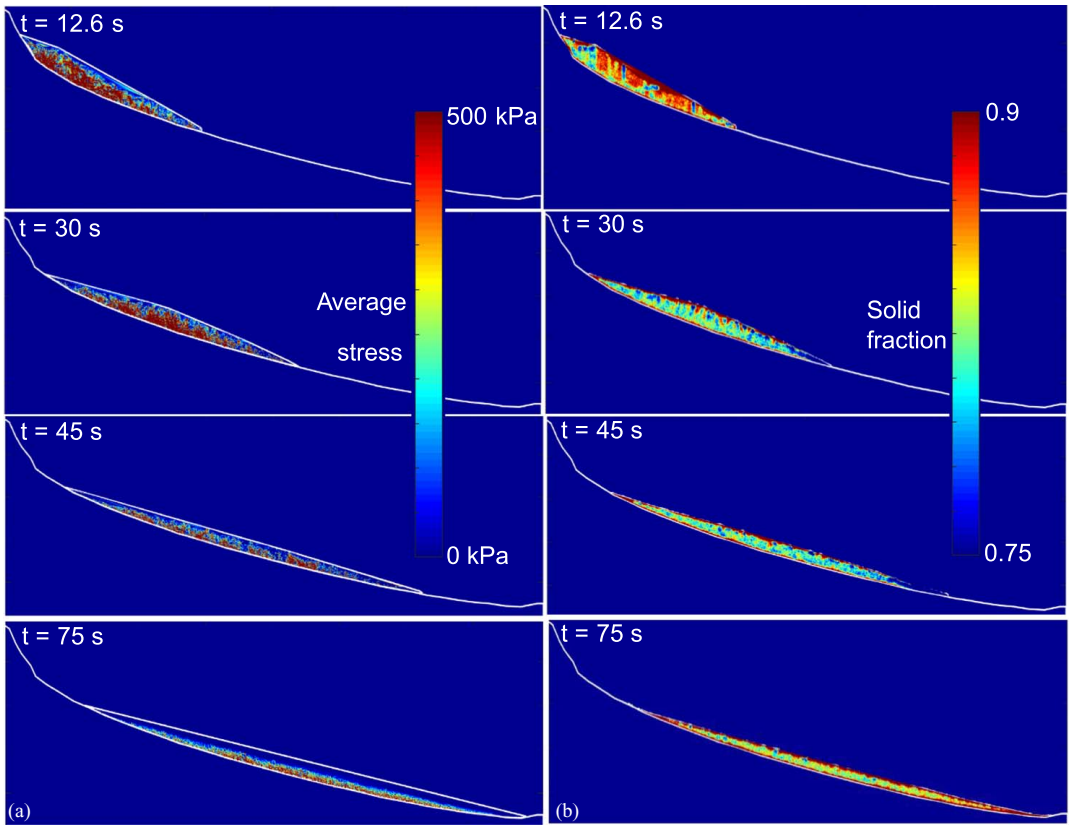

Fig. 10. Evolution of the interpolated: (a) average stress; and (b) solid concentration fields within the avalanche at different time stamps.

particles, n_v. The solid fraction is then defined in terms of the total representative volume V_{tot} within the nonconvex envelop, and the volume V_m of granular material inside the V_{tot}. To account for the fact that the increase in the number of particles inside the representative volume can reduce the inaccuracy, the n_v was chosen to be 50 in this study. The solid fraction is then calculated using

$$s = \frac{V_m}{V_{\text{tot}}} \tag{5}$$

The solid fraction pattern in the sliding mass [Fig. 10(b)] is spatially synchronized with the fracturing initiation, propagation, and coalescence (Fig. 9), and the areas of low solid fraction accord well with the ones experiencing a substantial amount of disintegration. In addition, the distribution of solid fraction in the avalanche can be a dynamic indicator for the fragmented flow, that is, first, the rock blocks are tightly connected by the bonds, forming a high solid concentration. Then, as the ground shaking intensity increases, bond breakages accumulate gradually to form a connected fragmented granular layer beneath the translating slope mass (see Fig. 9). This may lead to the more pronounced low solid fraction as the avalanche develops, promoting the subsequent landslide propagation [see Fig. 10(b)]. Concurrently, the front head of the granular body is also observed to possess the lowest solid concentration, which infers that an increasing number of solid particles within this region become dilute and easily jump away from the main body as shown in Fig. 10(b) (at time $t = 30$ s and $t = 45$ s). Finally, as the fragmented flow accumulates and deposits ($t = 75$ s), the granular body transits to possess a high solid fraction. This can be explained by the fact that the distribution of the solid fraction in the avalanche corresponds well with the dilation and compaction. The dilation is found to start at the base of the avalanche, and propagates through the entire mass as the avalanche develops. After cracking, fracturing, and deforming under the action of gravity and seismic forces, the bonded granular system is disintegrated into a clast and fine-grained matrix. This process results in continuous rearrangement and recompaction as the avalanche loses momentum and particles are progressively deposited in the runout area.

Energy Regime and Rock Damage

Evaluation of the energy regime of the rock avalanche is helpful for understanding the mechanism of rock fragmentation and the kinetic characteristics of rock fragments. Following Utili et al. (2015) and Zhao et al. (2017), the potential energy of the rock mass, E_p, is defined as follows with respect to a reference point, in this analysis, the reference point is the origin as shown in Fig. 5:

$$E_P = \sum_{i=1}^{N} m_i g h_i \tag{6}$$

where N = the total number of particles in the sliding body; m_i and h_i = the mass and height of each particle in the body. It is worthwhile to note, the E_P is also the total energy of the granular system in the sliding body, E_0, before downward movement.

The energy input due to earthquake waves acting on the boundaries is represented by

$$E_w^j = E_w^{j-1} + \sum_{i=1}^{N} F_w \Delta U_w \tag{7}$$

where E_w^j and E_w^{j-1} = the total accumulated work done by all walls on the assembly at the current and previous time steps; F_w = resultant force acting on the wall; ΔU_w = the applied displacement occurring during the current time step.

From the law of conservation of energy, the energy balance equation is typically

$$E_0 + E_w(t) = E_p(t) + E_{\text{strain}}(t) + \bar{E}_{\text{bstrain}}(t) + E_k(t) + E_f(t) + E_\mu(t) + E_\beta(t) \quad (8)$$

As shown in Fig. 11, before the earthquake wave propagates, the system has only potential energy and no energy is dissipated. As the flow develops, different types of energies (potential energy, kinetic energy, elastic energy, and dissipated energy) inside the granular mass evolve. When the avalanche develops with the combined effect of gravity and seismic forces, the potential energy decreases and the kinetic energy increases due to particle movements. The sum of the kinetic and potential energies during the avalanche is not equal to the total energy E_0 due to energy dissipation. Causes of energy dissipation are related to base friction, granular mass contact friction, and inelastic collisions. Detailed calculations of elastic strain (E_{strain}) and bond strain energies ($\bar{E}_{\text{bstrain}}$), kinetic energy (E_k), cumulative energy dissipated by friction (E_μ), and viscous damping (E_β) can be found in the documentation of Itasca Consulting Group (2014).

At the initial acceleration stage, the energy dissipation rate is found to be low. Afterward, in the high-speed runout phase, dynamic collisions among the fragments are intensified, which results in a sharp increase in the rate of energy dissipation before the fragmented flow transits to the low-speed deposition phase characterized by the gradual decreasing rate in energy dissipation. Ultimately, all the total energy E_0 is dissipated by friction (56.1%) and by collisions (43.9%). It is worth noting that although energy dissipation by breaking bonds is less significant in the deposition stage, particle breakage still plays a major role in the dissipation process as it creates additional degrees of freedom for the interparticle motion, which in turns facilitates friction dissipation. Similar conclusions have been reached by Bolton et al. (2008) and Ma et al. (2016) for breakable granular materials. Low fragmentation energy input in disintegrating the rock mass has been documented by Locat et al. (2006), Crosta et al. (2007), and Zhao et al. (2017).

In the analyses, the damage ratio (D) (Thornton et al. 1996) has been used to quantify rock fragmentation intensity, which is defined as the ratio of the number of broken bonds under the combined effect of gravity and seismic forces to the total number of bonds at initial static state. According to Fig. 12(a), it can be seen that the damage ratio increases rapidly characterized by the rapid cumulation of energy released by all bond breakages as the avalanche enters the high-speed runout phase. The subsequent sliding and collision of fragments in the low-speed deposition phase leads to an additional 3% of bond breakage. From the point of view of fragmentation energy, for the entire landsliding process, microtension failure occurs at a higher rate in comparison with microshear failure and plays a dominant role in the initiation of slope instability. Results show that the dissipated energy by fragmentation follows a linearly increasing trend similar to that of the damage ratio [Fig. 12(b)].

The degree of fragmentation shown in F_D provides a measure for the damage that the material has experienced (Haug et al. 2016).

$$F_D = \frac{M}{m_{\max}} \quad (9)$$

where M = the mass of the sample; and $m_{\max}$ = the mass of the largest fragment.

A value of $F_D = 1$ reflects a completely intact sample, while an increasingly value reflects an increasingly fragmented avalanche mass. In this study, F_D started from a value higher than 1, because of the existence of joint sets that influence the integrity of the avalanche body.

Fig. 12(c) shows how the degree of fragmentation (F_D) is related to damage ratio (D) for the rock avalanche. According to the plots, it is apparent that the degree of fragmentation (F_D) is rarely found

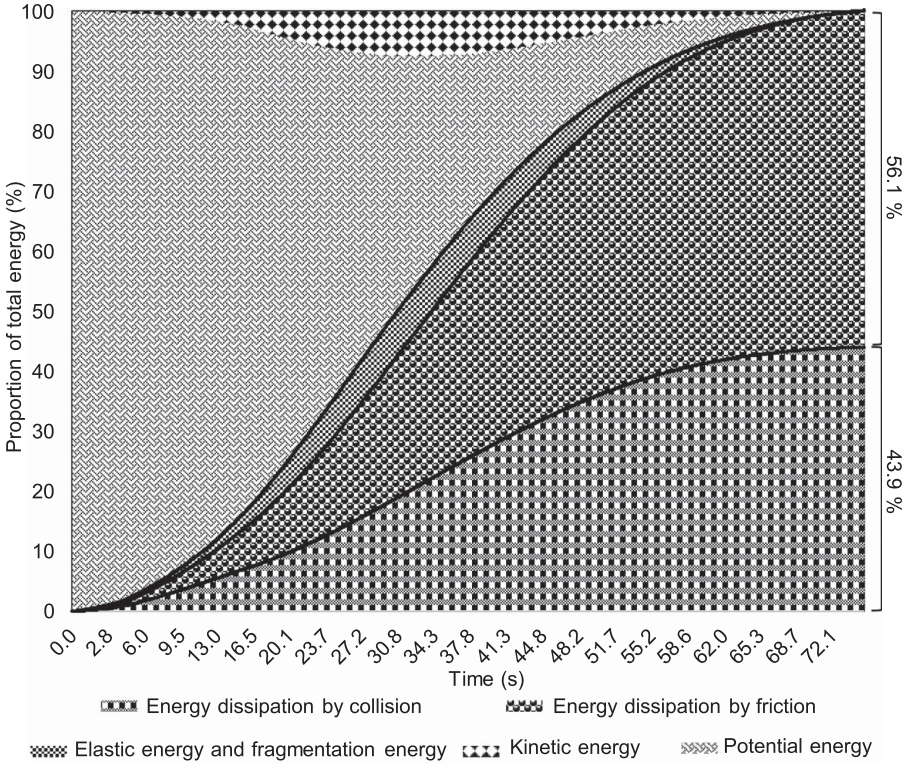

Fig. 11. Energy transfers resulting from the analysis of the rock avalanche.

Int. J. Geomech., 2020, 20(9): 04020157

to undergo a significant increase in rate until the damage ratio (D) reaches 0.2. Then it starts an immediate increase before the damage ratio (D) increases to 0.7, following a sharp increase to peak value when the damage ratio (D) reaches 0.74. It indicates the development of rock damage induces a large amount of fractures within the rock avalanche. Consequently, fractures can nucleate and grow to completion quickly, leading to relatively small fragments, and the corresponding degree of fragmentation (F_D) rises immediately to a high value. As presented in Fig. 12(d), it is interesting to note that the evolution of fragment number follows a similar trend to that of the landslide overall velocity [see Fig. 8(a)]. This phenomenon is expected as the landslide initiation and propagation promote the disintegration of the jointed rock mass within the slope with an obvious increase of medium and large fragments. Subsequently, continuous rapid dynamic avalanching motion in response to the increased seismic intensity may work to disaggregate the entire avalanche, which leads to the coarse fragments being completely broken to fine-grained particles, inducing a continuous decrease in fragment number. In addition, these fine-grained particles play an important role in the absorption of a large portion of the kinetic energy of incoming fragments. Thus, the presence of shattered and disaggregated clasts with relatively larger size can be preserved from the collision and freefall motions during the landslide propagation and deposition [see Figs. 15(c and d)].

Lubrication Mechanism and Friction Reduction

As stated by Campbell (1989) and Cleary and Campbell (1993), for the completely fragmented granular system, particles at the base are intensely agitated with frequent collisions and could act as a lubricating layer to reduce the overall effective friction of the fragmenting grain flow. The intensity of particle agitation can be quantified by the vibrational and rotational granular temperatures (Campbell 2006) and be defined as

$$v_x^i(t)' = v_x^i(t) - \overline{v_x^i(t)} \tag{10}$$

$$v_y^i(t)' = v_y^i(t) - \overline{v_y^i(t)} \tag{11}$$

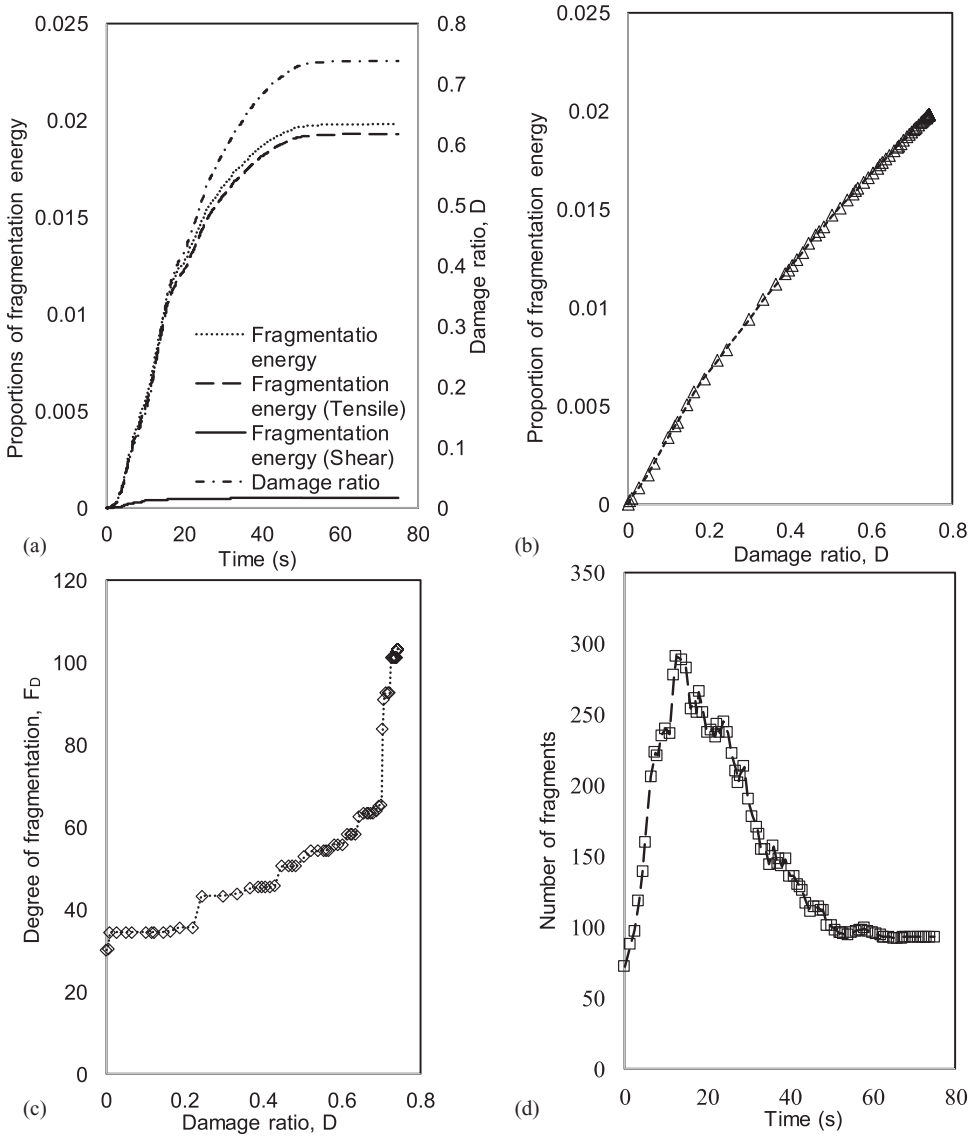

Fig. 12. (a) Changes in fragmentation energy with the time; (b) fragmentation energy versus damage ratio; (c) degree of fragmentation versus damage ratio; and (d) number of fragments evolution.

Int. J. Geomech., 2020, 20(9): 04020157

$$\omega^i(t)' = \omega^i(t) - \overline{\omega^i(t)} \tag{12}$$

where translational velocity components $v_x^i(t)$, $v_y^i(t)$ and angular velocity component $\omega^i(t)$ of the selected i-th particle in the selected spherical region Ω_i can be divided into the mean velocity components $\overline{v_x^i(t)}$, $\overline{v_y^i(t)}$, and $\overline{\omega^i(t)}$ and fluctuating parts $v_x^i(t)'$, $v_y^i(t)'$, and $\omega^i(t)'$.

The mean velocity components $\overline{v_x^i(t)}$, $\overline{v_y^i(t)}$, and $\overline{\omega^i(t)}$ can be attained by averaging the velocities of particles surrounding the selected i-th particle in the selected spherical region Ω_i as

$$\overline{v_x^i(t)} = \frac{1}{n}\sum_{j=1}^{n} v_x^j(t) \tag{13}$$

$$\overline{v_y^i(t)} = \frac{1}{n}\sum_{j=1}^{n} v_y^j(t) \tag{14}$$

$$\overline{\omega^i(t)} = \frac{1}{n}\sum_{j=1}^{n} \omega^j(t) \tag{15}$$

$$(x_j - x_i)^2 + (y_j - y_i)^2 \le r^2 \tag{16}$$

where r = the radius of the selected spherical region Ω_i. In this study, the neighborhood size $2r$ is set to $5d_{50}$ according to the Zhou et al. (2016).

Hence, the vibrational $T_V^i(t)$ and rotational $T_R^i(t)$ granular temperatures representing the intensity of particle exchange analogous to a thermodynamic temperature are calculated from the velocity fluctuations and expressed as

$$T_V^i(t) = \frac{1}{2}[(v_x^i(t)')^2 + (v_y^i(t)')^2] \tag{17}$$

$$T_R^i(t) = (\omega^i(t)')^2 \tag{18}$$

The distributions of $T_V^i(t)$ and $T_R^i(t)$ are presented in Figs. 13 and 14, respectively, and demonstrate that a layer of agitated particles does exist at the slope base during the emplacement of a rock avalanche, which can effectively reduce the landslide friction with increased mobility. It indicates that during landslide propagation,

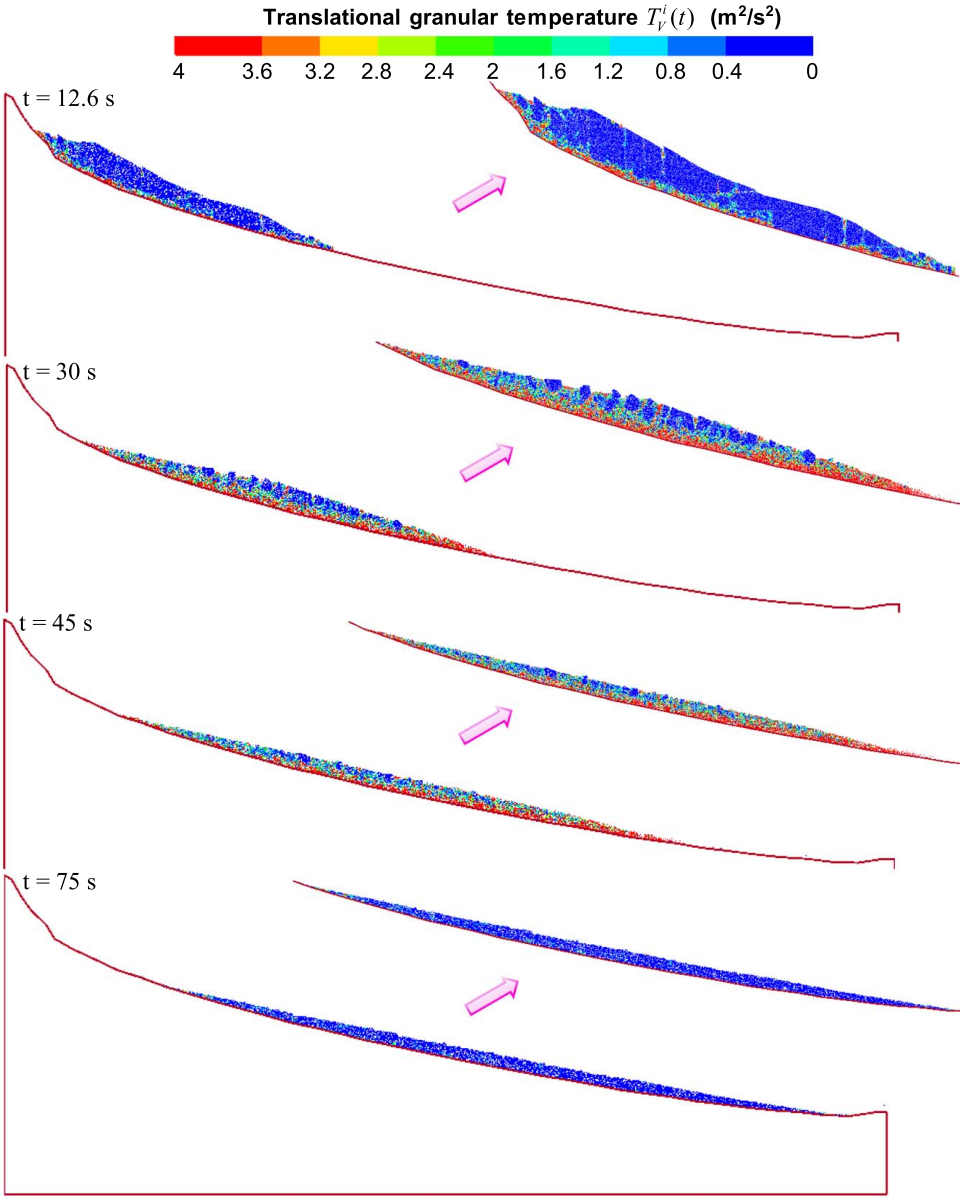

Fig. 13. The distribution of translational granular temperatures $T_V^i(t)$ at different time stamps.

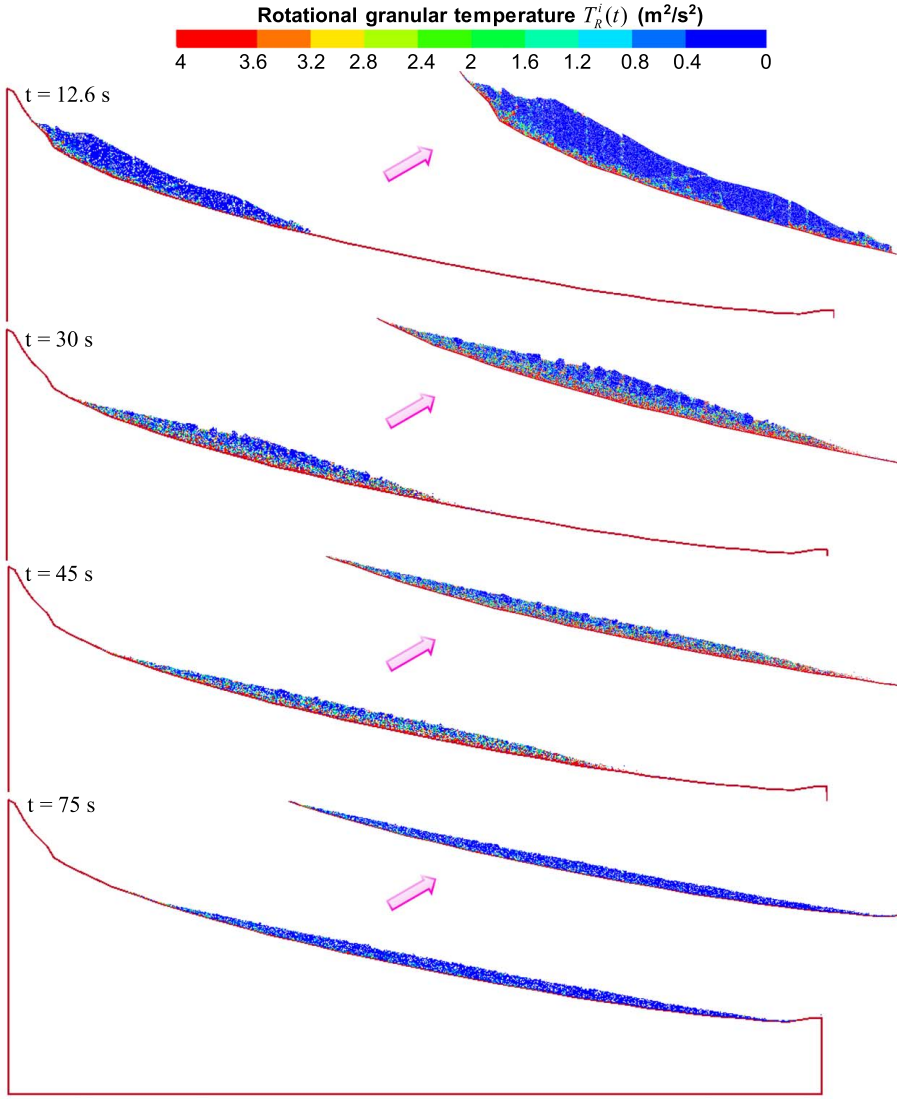

Fig. 14. The distribution of rotational granular temperatures $T_R^i(t)$ within the avalanche at different time stamps.

extensive fluctuations of vibrational and rotational granular temperatures are activated in the basal layer where the intense shearing promotes particle rearrangement characterized by vigorous particle agitations (see $t = 30$ s in Figs. 13 and 14). This observation agrees well with numerical results of Zhao and Crosta (2018), who calculated the evolution of granular temperature of an estimated 25 m thickness of granular basal layer and demonstrated that the generated particle vibrations are responsible for the apparent reduction of friction in long-runout landslides, though they did not show how the granular temperatures exactly distributed within the slope mass. It is worth noting that the lack of obvious enhancement of granular temperatures and fluctuations around the coarse fragments reflects that continuous fragmentation produces a thick layer of dispersed grains near the bottom which can to some extent lubricate the landsliding motion but also significantly consumes a large portion of energy from the incoming large rock fragments. This indicates that the large boulders at the surface were passively carried by the finer material below during movement.

These observations match some of the well-documented field data of long-runout landslides reported in Dufresne et al. (2010) and Zhang et al. (2019). In addition, a low solid density area can be observed at the basal shearing layer [see Fig. 10(b)], which further demonstrates that because of frequent intensive collisions, the overburden acting on the shearing layer can be counteracted. Therefore, the enhanced granular temperatures allow for the occurrence of dilation in the basal facies characterized by the sparse solid fraction and the increased mobility, which is consistent with the observations that the entire granular flow is levitated above the vibrating base by a layer of highly energetic particles (Lim 2010; Zhou and Sun 2013). After the cessation of seismic shakings, the landslide propagates to the low-speed deposition phase, therefore the entire granular body exhibits a gradually attenuating fluctuation intensity (see $t = 75$ s in Figs. 13 and 14). This phenomenon accords well with the statement that the granular temperature can dissipate or vanish rapidly due to interparticle collisions when external energy stops (Campbell 1990).

Fragmentation and Fragment Distribution

Numerical simulations of the fragmentation process during the rock avalanche are shown in Fig. 15 (the hue scale in the figure is logarithmic). As the ground shaking accelerates, bond breakages accumulate gradually such that the fracture network separates the sliding body into a large number of fragments of comparable sizes (see Fig. 15 at $t = 12.6$ s). Then, as the intense seismic shakings proceed, the subsequent landslide propagation and deposition

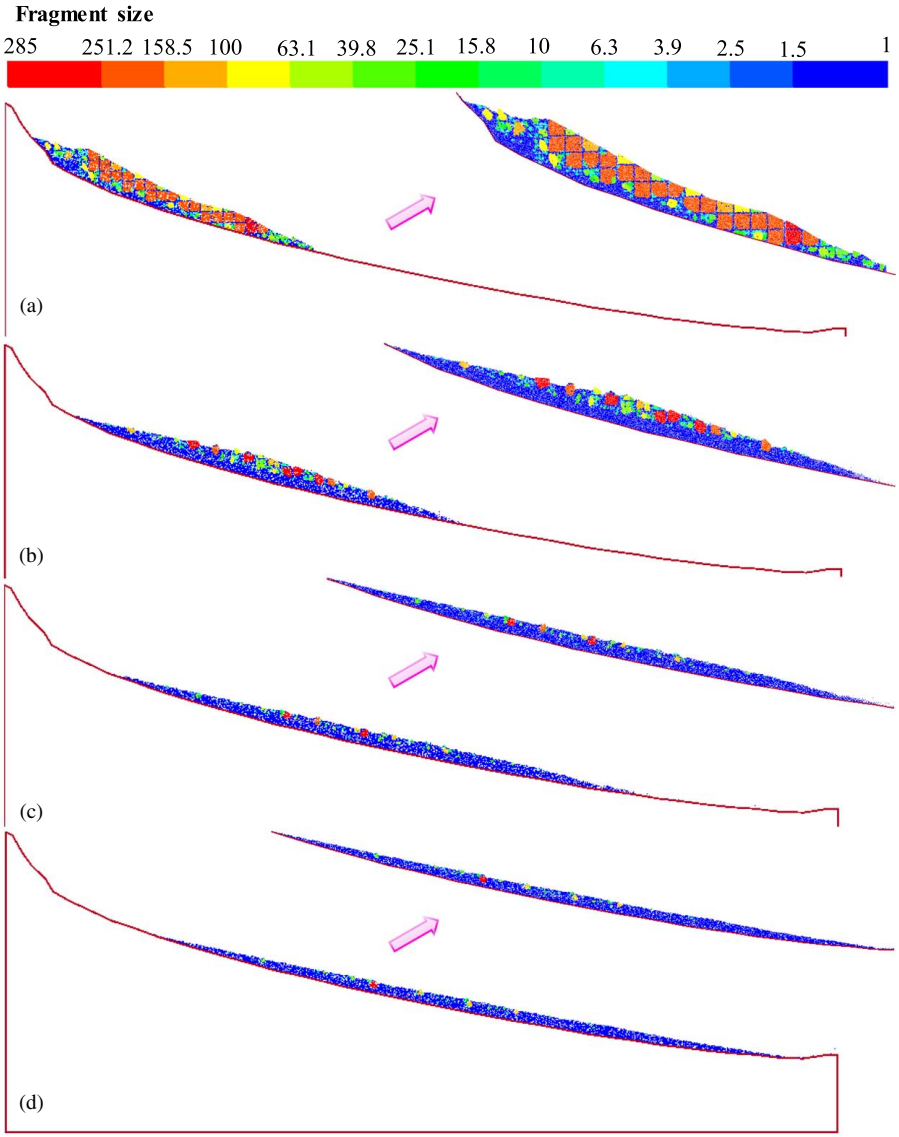

Fig. 15. Changes in fragment size at different time stamps: (a) $t = 12.6$ s; (b) $t = 30$ s; (c) $t = 45$ s; and (d) $t = 75$ s.

cause more damage to the slope mass leading to intensive cracking, especially near the front and rear regions, reflected by the continuous enlargement of fine-grained materials, shown in Figs. 15(b and c). The final low-speed deposition phase [see Fig. 15(d)] shows that the major part of the slope mass has been intensely disaggregated and large boulder content is more abundant in the middle areas, while the fine grains are predominant in distal locations. The distribution pattern of large rock blocks in the final deposits agrees well with the field observations (Hu et al. 2013) that the middle region contains many larger boulders and blocks. In addition, it is worth noting that the difference of fragmentation between Figs. 15(c and d) is not significant; this can be explained by the fact that accumulation of fine-grained particles reduces the collision rate between the coarser fragments and partially inhibits the disintegration of the debris in the avalanche (Perinotto et al. 2015).

To obtain the fragment size distribution, the characteristic fragment size is defined as

$$d = \sqrt{V_f / V_0} \tag{19}$$

where V_f = the volume of a fragment (calculated as the total volume of particles in the fragment); and V_0 = the volume of the rock mass within the source area at initial static state.

The cumulative distribution of fragmented rock mass can be fitted using a two-parameter Weibull equation. This distribution, which is equivalent to the Rosin-Rammler distribution (Rosin and Rammler 1933), has been successfully used in characterizing the fragment size of spherical solid grains (Ma et al. 2018) and rock grains (McSaveney 2002; Ma et al. 2017; Shen et al. 2017). The two-parameter Weibull distribution can be expressed as

$$P = 1 - \exp\left[-\left(\frac{d}{d_c}\right)^{\nu}\right] \tag{20}$$

where d_c and ν = fitting parameters. Here, ν indicates the width of the distribution, and larger values of ν correspond to narrower distributions.

Fig. 16(a) shows the volume-based cumulative fragment size distributions and the corresponding fitting curves of fragmented rock mass at progressive earthquake loading times. It can be seen that the two-parameter Weibull equation provides a good description of the simulated fragment size distribution. As noted earlier, d_c can be used as an index to quantify the content of fines in the fragmenting system (Ma et al. 2017). Therefore, a low d_c value is expected if the fragmenting system consists of a high level of fines. The parameter ν is a measure of the spread of the fragment

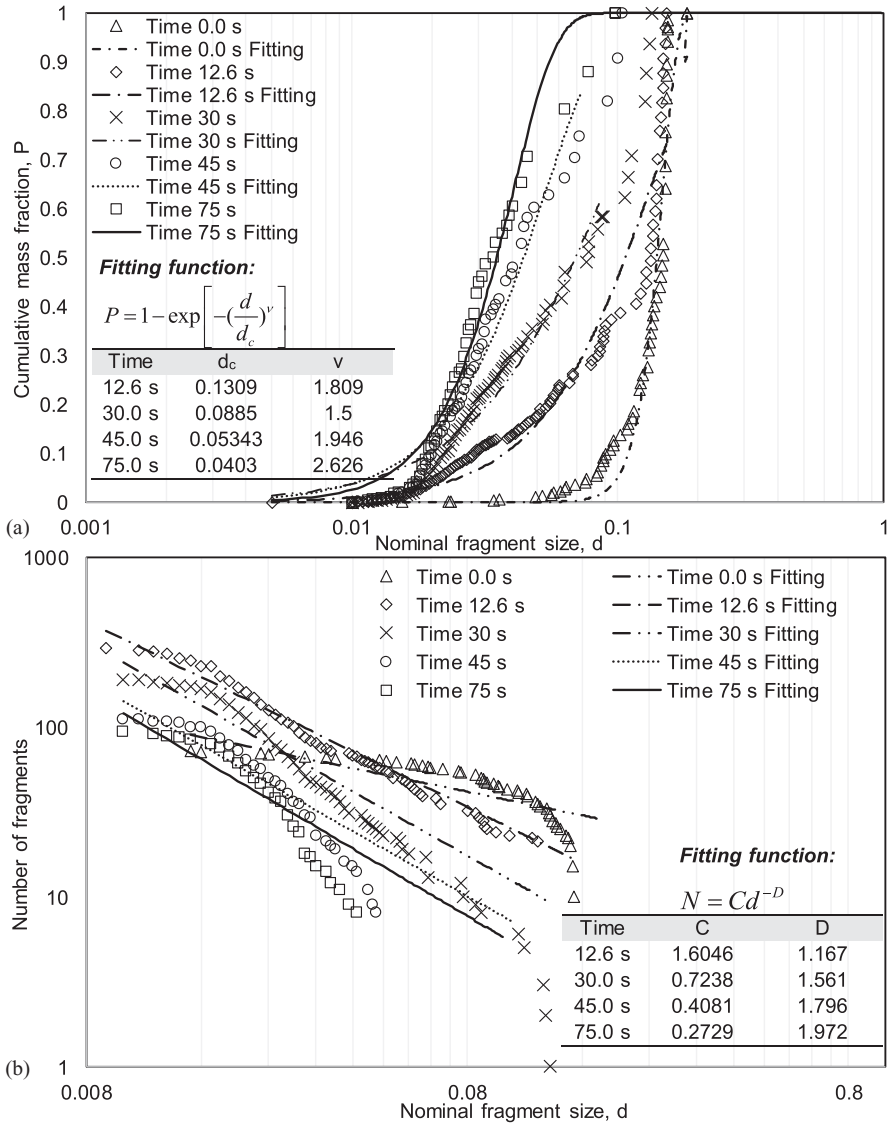

Fig. 16. (a) Relationship between cumulative mass fractions and fragment sizes for increasing loading time; and (b) fractal distributions of fragment sizes for increasing loading time.

size distribution, where the distribution is narrower for a larger value of v. For fragment size distributions weighted by fragment mass [Fig. 16(a)], the parameter d_c decreases with landslide propagation (see Fig. 9). It reflects that fragment size reduction obviously takes place in the course of downslope movement. It is consistent with observations that the fragmented debris in the landslide deposits is consecutively reduced in grain size along the transport path, which has been reported in some well-documented numerical and field studies (Perinotto et al. 2015; Zhang et al. 2016, 2019). The parameter v generally increases indicating that a narrower fragment size distribution is generated, except at the time of 30 s then decreases from 1.809 to 1.5, resulting in a wider span of fragment regime [Fig. 16(a)]. This exception occurs mainly due to the transition [Fig. 16(a)] from the phase of early acceleration ($t < 10$ s) to the phase of low-speed deposition ($t > 45$ s). This can be explained by the fact that early stages of emplacement contribute the most to the rock mass break-up. Relatively minor fragmentation occurs in the weak solid structures resulting in particle size distribution that spans a narrower range around the relatively large particles. Subsequently, the ground shaking intensity increases, leading to the propagation of cracks along the joint sets and the separation of fragments. When the low-speed deposition phase is reached, the majority of the slope mass is fragmented into fine-grained particles which causes the size distribution to be dominated by relatively small grain sizes. It is found that, at all examined time stamps, the middle part of the fragment size distribution is almost linear within the range of 0.015 to 0.05. In addition, the distributions fluctuate at 12.6 s, indicating the presence of large unbroken pieces, which can be corroborated by the sedimentary fabric within the deposit as shown in Fig. 15 at $t = 12.6$ s.

The fragments produced by weathering, abrasion, impact, and geological loading often satisfy a fractal condition over a wide range of scales (Turcotte 1986). Therefore, it is necessary to examine the fractal characteristics during the entire transport phase of the avalanche [see Fig. 16(b)].

A fractal character can be described by the power–law relationship between the number and size as

$$N = Cd^{-D} \tag{21}$$

where N = the number of fragments with a characteristic linear dimension larger than d; C = a proportional constant; and D = the fractal dimension. Then, the absolute value of D (the slope of the

best-fit line on a log–log scale) is equivalent to the fractal dimension of the particle size distribution (Turcotte 1986). The higher the value of D, the more graded the particle size distribution and the larger the number of fine particles (Crosta et al. 2007).

Fig. 16(b) illustrates that with landslide propagation and deposition, more and more fines are produced, reflected by an increase in the value of fractal dimension, D. The larger the value of the fractal dimension, the wider the range of particle size. In addition, the fractal dimension, D, of a particle size distribution increases sharply (up to 30 s) then slows down significantly with increased duration of movement, which infers that the fragmentation energy during the rapid runout movement is quite high [see Fig. 12(a)] before reaching the low-speed deposition phase. This is in agreement with previous field and experimental observations (Crosta et al. 2007), which concluded that fractal dimension initially increases sharply before slowing down with the range of duration for rock avalanches. It is worth noting that power law prevails in the range of small to intermediate size regimes of all the distributions, and a more complete fitting is observed when the landslide has not experienced an intense fragmentation process, as illustrated in Fig. 16(b). It is apparent that fractal characteristics significantly change with respect to rock avalanche dynamics. During the emplacement process, fractal dimension changes and particle assemblages will either be destroyed or preserved, as illustrated in Fig. 4(c) and confirmed by the numerical results in Fig. 15. This is also consistent with the field observations reported by Pollet and Schneider (2004), Crosta et al. (2007), Pedrazzini et al. (2013), Perinotto et al. (2015), and Wang et al. (2018). At the investigated time stamps, the intermediate fractal dimension is almost linear within nominal size that range from 0.009 to 0.03, which is justified well with the observations of the fragment size distributions weighted by fragment mass. This linearity indicates that the distribution of the fragment sizes has a fractal structure.

A statistical analysis is conducted to investigate the characteristics of fragment populations. It is apparent from Fig. 17 that the distribution of nominal fragment sizes in each examined

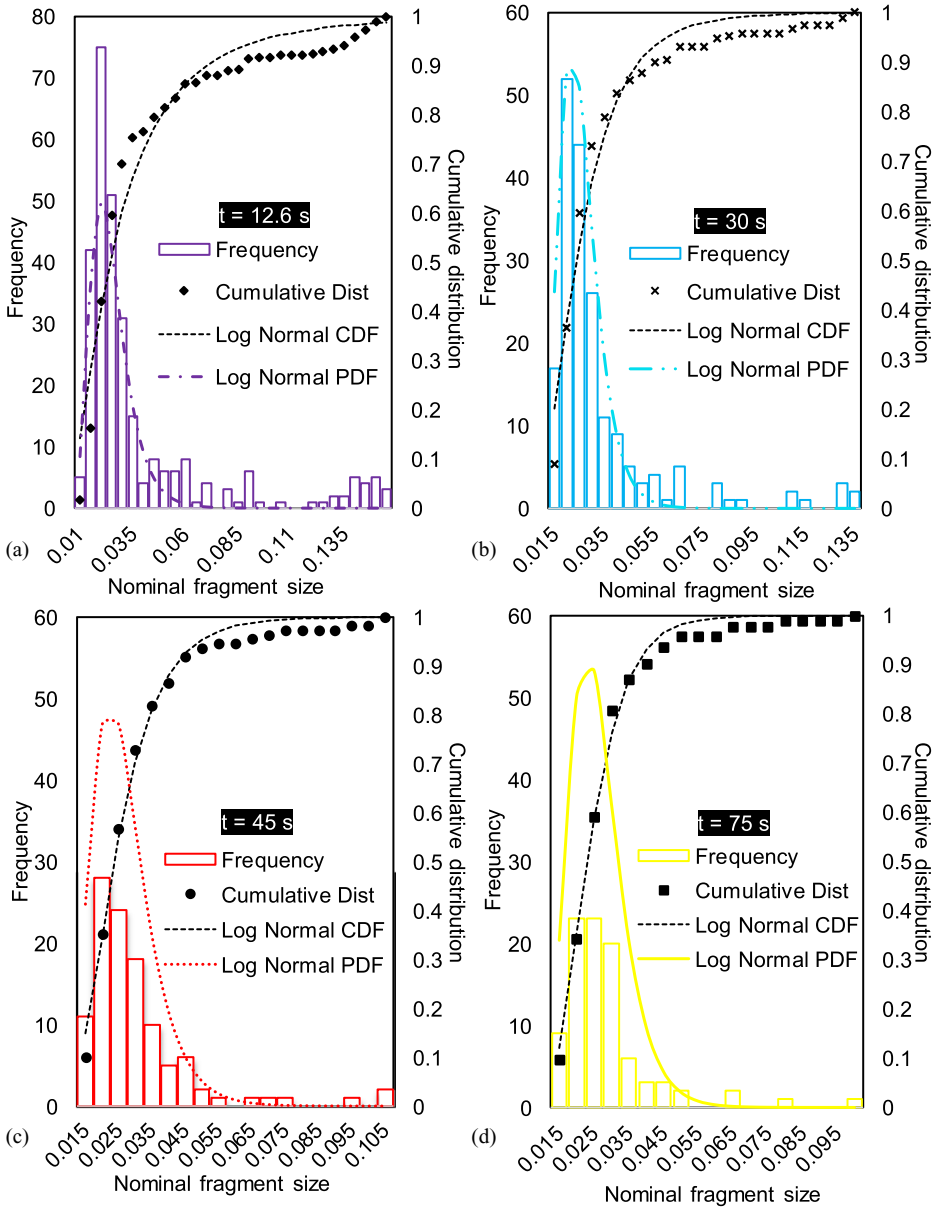

Fig. 17. Fragment size frequency distributions with corresponding log-normal approximations for the four investigated timestamps.

timestamps is asymmetric, being skewed toward the smaller sizes. Such a distribution lends itself to approximation of a log-normal distribution (Fityus et al. 2013). The cumulative distribution and probability density functions of the log-normal distribution are expressed by Eqs. (22) and (23), respectively:

$$F_X(x) = \frac{1}{2} + \frac{1}{2}\,\mathrm{erf}\left[\frac{\ln(x) - \mu}{\sqrt{2}\sigma}\right] \tag{22}$$

$$f_X(x) = \frac{1}{\sigma\sqrt{2\pi}x} e^{-(\ln x - \mu)^2/2\sigma^2} \tag{23}$$

where erf = the complementary error function; σ (the standard deviation) = the shape parameter which affects the general shape of the distribution; and μ (the mean) = the location parameter that controls the location on the x-axis.

As presented in Fig. 17, it is evident that most of the fragments distribute within a nominal fragment size range ($0.01 \le d \le 0.035$) being dominant at all examined time stamps although the differences are significant. The histograms of earlier time stamps (i.e., at time of 12.6 and 30 s) show the largest quantity of fragments distributes around the nominal fragment size ($0.015 < d \le 0.02$), being far less frequent in comparison with other size ranges. As the avalanche transits into the low-speed deposition phase, the already fractured rock mass becomes further deteriorated into a number of smaller fragments, and the peak shown in the histograms between 0.015 and 0.2 gradually disappears and the difference in the size ranges becomes less obvious with more evenly distributed size ranges in $0.02 \le d \le 0.03$. In addition, too coarse fragments do not exist for low-speed deposition phase ($t = 75$ s), inferring a severe fragmentation of the rock mass during the avalanche transport induces a substantial reduction of clast size.

In advance of more detailed investigation on the mechanisms associated with the transport of a coseismic rock avalanche, a statistical analysis was carried out to examine the shape characteristics of the fragment populations by checking the fragment shape isotropy (see Fig. 18). The shape isotropy can be calculated using the square root of the ratio of the larger I_1 and smaller I_2 eigenvalues of the tensor of inertia of the 2D fragment shape (Timár et al. 2010). The tensor of inertia can be calculated as

$$I_{ij}^{\text{fragment}} = \sum_{d=1}^{N_d} (I_{ij}^d \delta_{ij} + m^d x_i^d x_j^d) \tag{24}$$

where each fragment contains N_d base disks of mass m^d and inertial tensor I^d relative to the disk local Cartesian axis; and δ_{ij} = Kronecker delta. The vector $\mathbf{x}^d$ is given by $x_j^d - x_j^{\text{fragment}}$, where $\mathbf{x}^d$ and $\mathbf{x}^{\text{fragment}}$ = vectors describing the constituent disk and fragment centroids, respectively.

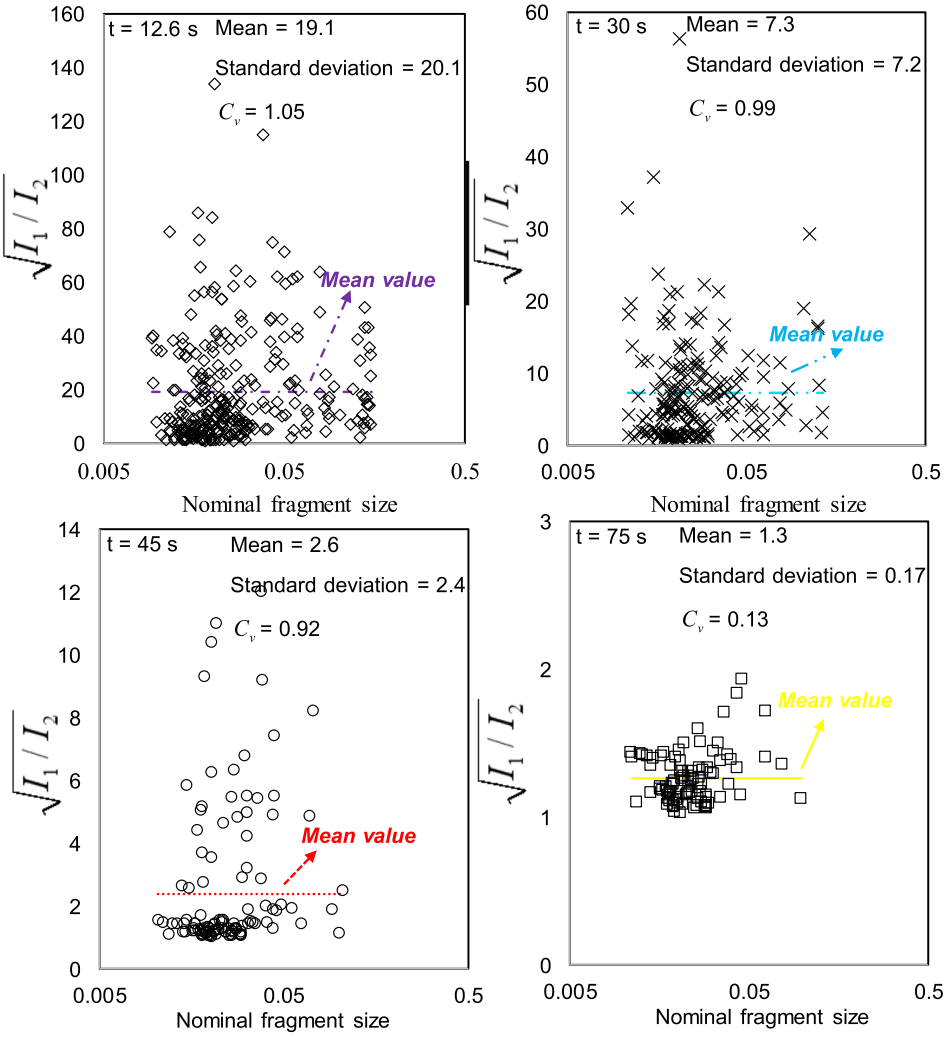

Fig. 18. Distributions of the square root of the ratio of the larger and smaller eigenvalues of the tensor inertia of the fragment shape for checking shape isotropy at different loading times.

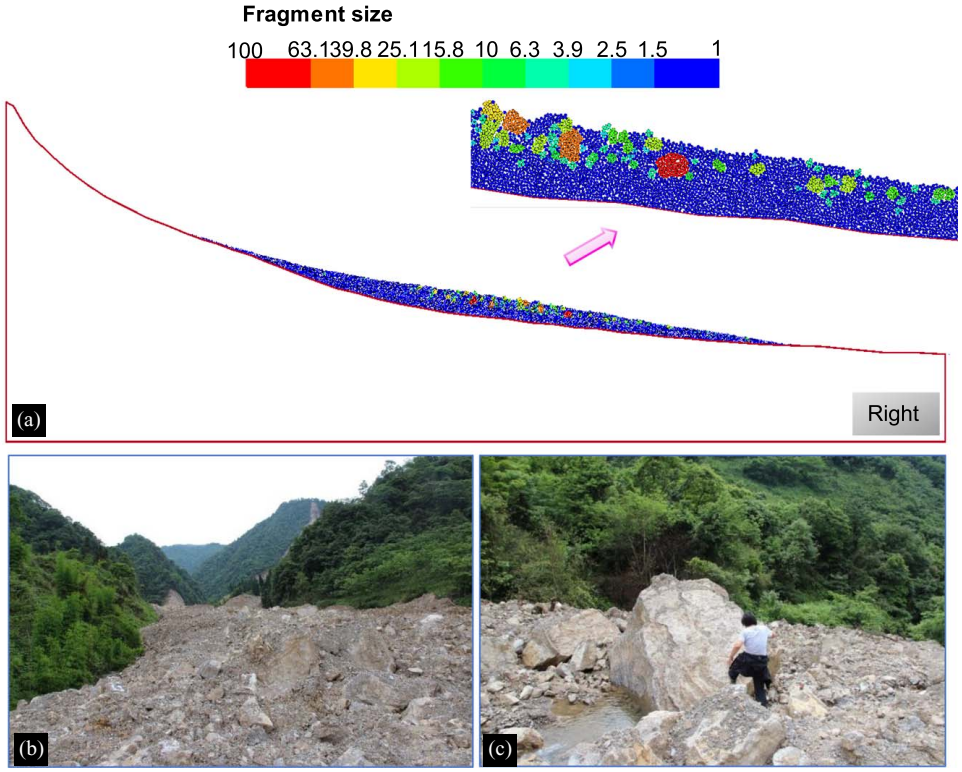

Fig. 19. Aspects of the fragmented deposits for the right stream of Tangjia avalanche: (a) discrete element numerical observation; (b) field investigation; and (c) large rock blocks observed only in deposits of the right stream.

The coefficient of variations (C_v = Standard deviation/mean) of $\sqrt{I_1/I_2}$ for the fragment shapes display significant variability in conjunction with emplacement and deformation of the rock avalanche in response to the ground motion. They are found to be significantly larger (1.05) at the initial time stamp ($t = 12.6$ s) and decrease from 0.99 to 0.92 during the rock movement. Finally, the mean and standard deviation of $\sqrt{I_1/I_2}$ are found to be 1.3 and 0.17, respectively, with a coefficient of variation of 0.13 when the avalanche comes to a final stop (see Fig. 18). A $C_v < 1$ is known as a relatively low variation, indicating a high level of fragment shape isotropy.

Significant deviation from the mean value of $\sqrt{I_1/I_2}$ is observed at earlier timestamps, in particular at the time of $t = 12.6$ s and $t = 30$ s. This is expected, as the ground shaking intensity increases, bond breakages continue gradually and cut through the slope mass to form coarse blocks. These freshly broken rock blocks have not yet undergone textural changes such as friction abrasion, continuous comminution and grinding. These textural changes are what make the particles more mature with a high degree of rounding and smoothness (Perinotto et al. 2015). The subsequent landslide propagation and deposition are found to cause more damages to the slope mass, as reflected by the gradual enlargement of damage zones and the increase in shape isotropy. This also resulted in an increase in the proportion of fine-grained matrix to coarse-grained blocks with distance. Although the fragment shape isotropy is relatively high at the final deposition stage, deviation from the mean value is observed around the large grain sizes; this suggests that both texturally immature (coarse blocks) and mature (fine particles) deposits form the landslide deposit. The similar behavior was also observed in other large-scale rock avalanches (e.g., Crosta et al. 2004, 2007). The reduction in variance of the distribution of shape isotropy parameter ($\sqrt{I_1/I_2}$) for the fragmented blocks can be interpreted as a signature of the dynamic disintegration that occurs continuously during the transport process and the presence of significant subsequent abrasion of newly fragmented blocks (stable distribution of $\sqrt{I_1/I_2}$ values).

As shown in Fig. 19(a), the sizes of fractured coarse blocks within deposition of the right stream of rock avalanche remain much larger than that of the left stream deposition. This is in good agreement with the sedimentary fabric found at the site. Compared with the deposits of the left stream [see Fig. 4(c)], the field investigations demonstrate that deposition of the right stream of the Tangjia Valley rock avalanche consists of a larger quantity of coarse boulders and blocks, as shown in Fig. 19(b), and even huge blocks up to 3 m in size [see Fig. 19(c)] can be observed in the deposit of the right stream whereas they are not found in the deposit of the left stream. Furthermore, the maximum diameter of the deposited boulder within the accumulation zone in the right stream is found to be 3 m, whereas the maximum diameter found in the left stream of the rock avalanche is found to be about 2 m. This can be explained by the fact that the left stream detaches and moves down a steep slope, which facilitates a higher-speed movement and fosters more rock fragmentation and finer deposits.

Conclusion

In this study, DEM analyses that incorporate spatial interpolation techniques and statistical analyses were performed. The results provided new insights on the characteristics of dynamic rock fragmentation and the mechanisms governing the transport kinematics of a coseismic landslide, including trajectory motion, fracture propagation, the evolution of stresses, and the solid concentration. Compared with previous analyses, the novelty is in portraying evolution of granular temperature and solid fraction to identify and interpret the dilative behavior associated with particle dynamic

fragmentation. In addition, the original application of fragment shape isotropy for highlighting the deposition of the rock avalanche demonstrates that the fragmentation process continues throughout the entire runout. In addition, the observed features from field investigations are used to verify the validity of the numerical model. The major findings of this study are summarized as follows:

1. In the initiation of the landslide, earthquake load plays a pivotal role in fracturing and fragmentation of the rock mass leading to slope destabilization. This is reflected in the internal rock damage that occurs and propagates gradually along the basal failure plane.
2. During the coseismic landslide propagation and deposition, the interpolated stress fields within the avalanche reveals a stress concentration in the basal layer of the slope mass, where rock fragmentation and deformation are likely to occur, inducing a dilution of solid concentration. The evolution of solid concentration within the slope mass is found to accord well with the dilation and compaction of the dynamically fragmented flow process. The granular body has relatively pronounced solid concentrations as it starts with a tightly bonded contact network before dilation occurs. This is attributed to the stretching and thinning of the avalanche body with the slope mass transforming into a fully developed fragmented flow, inducing reduction in bulk density of the avalanche body, in particular, the basal area and free surface, where the kinetic energy is greatly enhanced promoting high speed and long runout of the rock avalanche. Finally, a compaction follows as the avalanche loses momentum and gradually accumulates in the deposition area. Lack of stress at the top of the granular body with the relatively high solid concentration, contribute to the development of fractured large boulders found in large avalanche deposits.
3. During the high-speed motion of the sliding mass after detaching from the source area, an intensely sheared, dilute, and agitated layer spontaneously appears at the base of the slope mass promoting the occurrence of particle dynamic fragmentation in basal layer. This can further dilate and disperse the basal facies material allowing the solid concentration to decrease and flow mobility to increase.
4. Characteristics of fragmentation during rock avalanches are systematically analyzed in terms of the statistics of the fragment size and fractal dimensions. The two-parameter Weibull equation provides an adequate description of the simulated fragment size distributions. The variations d_c and ν indicate that the occurrence of rock disintegration during landslide initiation and propagation is characterized by an obvious increase of various sizes of fragments, causing the fragment size distribution to span a wider range first, then gradually as the slope damage zone propagates from the failure plane to the internal slope mass. Consequently, the entire avalanche body experiences severe fragmentation, which promotes a large proportion of fragments that has been broken into fine-grained particles, inducing an increasingly narrower fragment size distribution.
5. The generated fragment shapes tend to be well isotropic during the avalanche deposition process. The coefficient of variations of the inertia tensor of $\sqrt{I_1/I_2}$ changes significantly to lower values. This reflects the textural maturation by fragmentation with considerable shearing and continued friction abrasion during the transport process.

Acknowledgments

This research is supported by the Natural Sciences and Engineering Research Council of Canada (NSERC). Financial support provided by McGill Engineering Doctoral Award (MEDA) to the first author is appreciated.

References

Antolini, F., M. Barla, G. Gigli, A. Giorgetti, E. Intrieri, and N. Casagli. 2016. "Combined finite–discrete numerical modeling of runout of the Torgiovannetto di Assisi rockslide in central Italy." *Int. J. Geomech.* 16 (6): 04016019. https://doi.org/10.1061/(ASCE)GM.1943-5622.0000646.

Bagnold, R. A. 1954. "Experiments on gravity-free dispersion of large solid sphere in a Newtonian fluid under shear." *Proc. R Soc. A* 225 (1160): 49–63. https://doi.org/10.1098/rspa.1954.0186.

Barla, M., G. Piovano, and G. Grasselli. 2011. "Rock slide simulation with the combined finite-discrete element method." *Int. J. Geomech.* 12 (6): 711–721. https://doi.org/10.1061/(ASCE)GM.1943-5622.0000204.

Bolton, M. D., Y. Nakata, and Y. P. Cheng. 2008. "Micro- and micro-mechanical behaviour of DEM crushable materials." *Géotechnique* 58 (6): 471–480. https://doi.org/10.1680/geot.2008.58.6.471.

Bowman, E. T., W. A. Take, K. L. Rait, and C. Hann. 2012. "Physical models of rock avalanche spreading behaviour with dynamic fragmentation." *Can. Geotech. J.* 49 (4): 460–476. https://doi.org/10.1139/t2012-007.

Calvetti, F., G. Crosta, and M. Tatarella. 2000. "Numerical simulation of dry granular flows: From the reproduction of small-scale experiments to the prediction of rock avalanches." *Riv. Ital. Geotech.* 22 (2): 21–38.

Campbell, C. S. 1989. "Self-lubrication for long run-out landslides." *J. Geol.* 97 (6): 653–665. https://doi.org/10.1086/629350.

Campbell, C. S. 1990. "Rapid granular flows." *Annu. Rev. Fluid Mech.* 22 (1): 57–90. https://doi.org/10.1146/annurev.fl.22.010190.000421.

Campbell, C. S. 2006. "Granular material flows: An overview." *Powder Technol.* 162 (3): 208–229. https://doi.org/10.1016/j.powtec.2005.12.008.

Campbell, C. S., P. W. Cleary, and M. Hopkins. 1995. "Large-scale landslide simulations: Global deformation, velocities and basal friction." *J. Geophys. Res.: Solid Earth* 100 (B5): 8267–8283. https://doi.org/10.1029/94JB00937.

Chang, K. J., and A. Taboada. 2009. "Discrete element simulation of the Jiufengershan rock-and-soil avalanche triggered by the 1999 Chi-Chi earthquake, Taiwan." *J. Geophys. Res. Earth Surf.* 114: F03003.

Chang, S. B., and S. M. Zhang. 2007. *Hand book of engineering geology*, 169–170. 4th ed. Beijing: China architecture & Building Press.

Cleary P. W., and C. S. Campbell. 1993. "Self-lubrication for long-runout landslides: Examination by computer simulations." *J. Geophys. Res.* 98: 21911–21924.

Crosta, G. B., H. Chen, and C. F. Lee. 2004. "Replay of the 1987 Val Pola Landslide, Italian Alps." *Geomorphology* 60 (1–2): 127–146. https://doi.org/10.1016/j.geomorph.2003.07.015.

Crosta, G. B., P. Frattini, and N. Fusi. 2007. "Fragmentation in the Val Pola rock avalanche, Italian Alps." *J. Geophys. Res.* 112: F01006. https://doi.org/10.1029/2005JF000455.

Davies, T. R. H. 1982. "Spreading of rock avalanche debris by mechanical fluidization." *Rock Mech.* 15 (1): 9–24. https://doi.org/10.1007/BF01239474.

Davies, T. R. H., and M. J. McSaveney. 1999. "Runout of dry granular avalanches." *Can. Geotech. J.* **36**: 313–320.

Davies, T. R. H., and M. J. McSaveney. 2009. "The role of rock fragmentation in the motion of large landslides." *Eng. Geol.* 109 (1–2): 67–79. https://doi.org/10.1016/j.enggeo.2008.11.004.

Davies, T. R. H., M. J. McSaveney, and K. A. Hodgson. 1999. "A fragmentation spreading model for long-runout rock avalanches." *Can. Geotech. J.* 36 (6): 1096–1110. https://doi.org/10.1139/t99-067.

De Blasio, F. V., and A. Elverhøi. 2008. "A model for frictional melt production beneath large rock avalanches." *J. Geophys. Res.* 113: F02014. https://doi.org/10.1029/2007JF000867.

Dufresne, A., T. R. Davies, and M. J. McSaveney. 2010. "Influence of runout-path material on emplacement of the Round Top rock avalanche, New Zealand." *Earth Surf. Processes Landforms* 35 (2): 190–201. https://doi.org/10.1002/esp.1900.

Dunning, S. A., W. A. Mitchell, N. J. Rosser, and D. N. Petley. 2007. "The Hattian Bala rock avalanche and associated landslides triggered by the Kashmir earthquake of 8 October 2005." *Eng. Geol.* 93 (3–4): 130–144. https://doi.org/10.1016/j.enggeo.2007.07.003.
Eisbacher, G. H. 1979. "Cliff collapse and rock avalanches (sturzstroms) in the Mackenzie Mountains, northwestern Canada." *Can. Geotech. J.* 16 (2): 309–334. https://doi.org/10.1139/t79-032.
Erismann, T. H., and G. Abele. 2001. *Dynamics of rockslides and rockfalls*. Berlin: Springer.
Feng, Z. Y., C. M. Lo, and Q. F. Lin. 2017. "The characteristics of the seismic signals induced by landslides using a coupling of discrete element and finite difference methods." *Landslides* 14 (2): 661–674. https://doi.org/10.1007/s10346-016-0714-6.
Fityus, S. G., A. Giacomini, and O. Buzzi. 2013. "The significance of geology for the morphology of potentially unstable rocks." *Eng. Geol.* 162: 43–52. https://doi.org/10.1016/j.enggeo.2013.05.007.
Gao, G., and M. A. Meguid. 2018a. "Modeling the impact of a falling rock cluster on rigid structures." *Int. J. Geomech.* 18 (2): 04017141. https://doi.org/10.1061/(ASCE)GM.1943-5622.0001045.
Gao, G., and M. A. Meguid. 2018b. "On the role of sphericity of falling rock clusters—Insights from experimental and numerical investigations." *Landslides* 15 (2): 219–232. https://doi.org/10.1007/s10346-017-0874-z.
Gao, G., and M. A. Meguid. 2018c. "Effect of particle shape on the response of geogrid-reinforced systems: Insights from 3D discrete element analysis." *Geotext. Geomembr.* 46 (6): 685–698. https://doi.org/10.1016/j.geotexmem.2018.07.001.
Garcia, F. E., and J. D. Bray. 2018. "Distinct element simulations of shear rupture in dilatant granular media." *Int. J. Geomech.* 18 (9): 04018111. https://doi.org/10.1061/(ASCE)GM.1943-5622.0001238.
Giacomini, A., O. Buzzi, B. Renard, and G. P. Giani. 2009. "Experimental studies on fragmentation of rock falls on impact with rock surfaces." *Int. J. Rock Mech. Min. Sci.* 46 (4): 708–715. https://doi.org/10.1016/j.ijrmms.2008.09.007.
Gong, B., and C. A. Tang. 2017. "Slope-slide simulation with discontinuous deformation and displacement analysis." *Int. J. Geomech.* 17 (5): E4016017. https://doi.org/10.1061/(ASCE)GM.1943-5622.0000746.
Habib, P. 1975. "Production of gaseous pore pressure during rock slides." *Rock Mech.* 7 (4): 193–197. https://doi.org/10.1007/BF01246865.
Haug, Ø. T., M. Rosenau, K. Leever, and O. Oncken. 2016. "On the energy budgets of fragmenting rockfalls and rockslides: Insights from experiments." *J. Geophys. Res.: Earth Surface* 121 (7): 1310–1327. https://doi.org/10.1002/2014JF003406.
Havenith, H. B., and C. Bourdeau. 2010. "Earthquake-induced landslide hazards in mountain regions: A review of case histories from Central Asia. An inaugural lecture to the society." *Geol. Belg.* 13 (3): 137–152.
Hoek, E., and E. T. Brown. 1997. "Practical estimates of rock mass strength." *Int. J. Rock Mech. Min. Sci.* 34 (8): 1165–1186. https://doi.org/10.1016/S1365-1609(97)80069-X.
Hoek, E., P. K. Kaiser, and W. F. Bawden. 2000. *Support of underground excavations in hard rock*. London: CRC Press.
Hu., X. W., C. Z. Gu, Y. B. Niu, J. X. Liang, C. Pan, J. L. Wu, J. H. Lin, D. C. Chen. 2013. "Debris flow characteristics and movement process of Dayanbeng landslide in Tianquan county triggered by "4·20" Lushan earthquake." [In Chinese.] *J. Sowthwest Jiaotong Univ*. 48 (4): 590–598.
Imre, B., J. Laue, and S. M. Springman. 2010. "Fractal fragmentation of rocks within sturzstroms: Insight derived from physical experiments within the ETH geotechnical drum centrifuge." *Granular Matter* 12 (3): 267–285. https://doi.org/10.1007/s10035-009-0163-1.
Itasca Consulting Group. 2014. *Particle flow code in two dimensions (PFC2D)*. Minneapolis: Itasca Consulting Group.
Keefer, D. K. 1994. "The importance of earthquake-induced landslides to long term slope erosion and slope-failure hazards in seismically active regions." *Geology* 10 (1–4): 265–284. https://doi.org/10.1016/0169-555X(94)90021-3.
Kent, P. E. 1966. "The transport mechanism in catastrophic rock falls." *J. Geol.* 74 (1): 79–83. https://doi.org/10.1086/627142.
Li, B., A. Xing, and C. Xu. 2017. "Simulation of a long-runout rock avalanche triggered by the Lushan earthquake in the Tangjia Valley, Tianquan, Sichuan, China." *Eng. Geol.* 218: 107–116. https://doi.org/10.1016/j.enggeo.2017.01.007.
Lim, E. W. C. 2010. "Granular Leidenfrost effect in vibrated beds with bumpy surfaces." *Eur. Phys. J. E* 32 (4): 365–375. https://doi.org/10.1140/epje/i2010-10637-8.
Locat, P., R. Couture, S. Leroueil, J. Locat, and M. Jaboyedoff. 2006. "Fragmentation energy in rock avalanches." *Can. Geotech. J.* 43 (8): 830–851. https://doi.org/10.1139/t06-045.
Ma, G., Y. D. Zhang, W. Zhou, T. T. Ngc, W. Qiao, and C. Xing. 2018. "The effect of different fracture mechanisms on impact fragmentation of brittle heterogeneous solid." *Int. J. Impact Eng.* 113: 132–143. https://doi.org/10.1016/j.ijimpeng.2017.11.016.
Ma, G., W. Zhou, X. L. Chang, and M. X. Chen. 2016. "A hybrid approach for modeling of breakable granular materials using combined finite-discrete element method." *Granular Matter* 18 (1): 7. https://doi.org/10.1007/s10035-016-0615-3.
Ma, G., W. Zhou, R. A. Regueiro, Q. Wang, and X. L. Chang. 2017. "Modeling the fragmentation of rock grains using computed tomography and combined FDEM." *Powder Technol.* 308: 388–397. https://doi.org/10.1016/j.powtec.2016.11.046.
McNamara, S. 2013. "Absorbing boundary conditions for granular acoustics." In *Proc., 3rd Int. Conf. on Particle Based Methods—Fundamentals and Application, PARTICLES 2013*, edited by M. Bischoff, E. Oñate, D. R. J. Owen, and P. Wriggers, 80–90. https://upcommons.upc.edu/handle/2117/188316.
McSaveney, M. J. 2002. "Recent rockfalls and rock avalanches in Mount Cook National Park, New Zealand." In *Vol. 15 of Catastrophic landslides: Effects, occurrence, and mechanisms: Reviews in engineering geology*, edited by S. G. Evans, and J. V. DeGraff, 35–70. Boulder, CO: Geological Society of America.
McSaveney, M. J., and T. Davies. 2009. "Surface energy is not one of the energy losses in rock comminution." *Eng. Geol.* 109 (1–2): 109–113. https://doi.org/10.1016/j.enggeo.2008.11.001.
Melosh, H. J. 1986. "The physics of very large landslides." *Acta Mech.* 64 (1–2): 89–99. https://doi.org/10.1007/BF01180100.
Meunier, P., N. Hovius, and A. J. Haines. 2007. "Regional patterns of earthquake-triggered landslides and their relation to ground motion." *Geophys. Res. Lett.* 34: L20408. https://doi.org/10.1029/2007GL031337.
Mollon, G., V. Richefeu, P. Villard, and D. Daudon. 2012. "Numerical simulation of rock avalanches: Influence of a local dissipative contact model on the collective behavior of granular flows." *J. Geophys. Res.: Earth Surface* 117: F02036. https://doi.org/10.1029/2011JF002202.
Pedrazzini, A., M. Jaboyedoff, A. Loye, and M. H. Derron. 2013. "From deep seated slope deformation to rock avalanche: Destabilization and transportation models of the Sierre landslide (Switzerland)." *Tectonophysics* 605: 149–168. https://doi.org/10.1016/j.tecto.2013.04.016.
Perinotto, H., J. L. Schneider, P. Bachèlery, F. X. L. Bourdonnec, V. Famin, and L. Michon. 2015. "The extreme mobility of debris avalanches: A new model of transport mechanism." *J. Geophys. Res.: Solid Earth* 120 (12): 8110–8119. https://doi.org/10.1002/2015JB011994.
Pollet, N., and J. L. M. Schneider. 2004. "Dynamic disintegration processes accompanying transport of the Holocene Flims sturzstrom (Swiss Alps)." *Earth Planet. Sci. Lett.* 221 (1–4): 433–448. https://doi.org/10.1016/S0012-821X(04)00071-8.
Potyondy, D., and P. Cundall. 2004. "A bonded-particle model for rock." *Int. J. Rock Mech. Min. Sci.* 41 (8): 1329–1364. https://doi.org/10.1016/j.ijrmms.2004.09.011.
Rosin, P., and E. Rammler. 1933. "Laws governing the fineness of powdered coal." *J. Inst. Fuel.* 7: 89–105.
Shen, W. G., T. Zhao, G. B. Crosta, and F. Dai. 2017. "Analysis of impact induced rock fragmentation using a discrete element approach." *Int. J. Rock Mech. Min. Sci.* 98: 33–38. https://doi.org/10.1016/j.ijrmms.2017.07.014.
Shen, W. G., T. Zhao, J. Zhao, F. Dai, and G. G. D. Zhou. 2018. "Quantifying the impact of dry debris flow against a rigid barrier by

DEM analyses." *Eng. Geol.* 241: 86–96. https://doi.org/10.1016/j.enggeo.2018.05.011.
Shreve, R. L. 1968. "Leakage and fluidization in air-layer lubricated avalanches." *Geol. Soc. Am. Bull.* 79 (5): 653–658. https://doi.org/10.1130/0016-7606(1968)79[653:LAFIAL]2.0.CO;2.
Stead, D., E. Eberhardt, and J. S. Coggan. 2006. "Developments in the characterization of complex rock slope deformation and failure using numerical modelling techniques." *Eng. Geol.* 83 (1–3): 217–235. https://doi.org/10.1016/j.enggeo.2005.06.033.
Tang, C., G. Ma, M. Chang, W. Li, D. Zhang, T. Jia, and Z. Zhou. 2015. "Landslides triggered by the 20 April 2013 Lushan earthquake, Sichuan Province, China." *Eng. Geol.* 187: 45–55. https://doi.org/10.1016/j.enggeo.2014.12.004.
Tang, C. L., J. C. Hu, M. L. Lin, J. Angelier, C. Y. Lu, Y. C. Chan, and H. T. Chu. 2009. "The Tsaoling landslide triggered by the Chi-Chi earthquake, Taiwan: Insights from a discrete element simulation." *Eng. Geol.* 106 (1–2): 1–19. https://doi.org/10.1016/j.enggeo.2009.02.011.
Thompson, N., M. R. Bennett, and N. Petford. 2009. "Analyses on granular mass movement mechanics and deformation with distinct element numerical modeling: Implications for large-scale rock and debris avalanches." *Acta Geotech.* 4 (4): 233–247. https://doi.org/10.1007/s11440-009-0093-4.
Thornton C., K. K. Yin, and M. J. Adams. 1996. "Numerical simulation of the impact fracture and fragmentation of agglomerates." *J. Phys. D: Appl. Phys.* 29: 424–435.
Timár, G., J. Blömer, F. Kun, and H. J. Hermann. 2010. "New universality class for the fragmentation of plastic materials." *Phys. Rev. Lett.* 104 (9): 095502. https://doi.org/10.1103/PhysRevLett.104.095502.
Turcotte, D. L. 1986. "Fractals and fragmentation." *J. Geophys. Res.* 91 (B2): 1921–1926. https://doi.org/10.1029/JB091iB02p01921.
Utili, S., T. Zhao, and G. T. Houlsby. 2015. "3D DEM investigation of granular column collapse: Evaluation of debris motion and its destructive power." *Eng. Geol.* 186: 3–16. https://doi.org/10.1016/j.enggeo.2014.08.018.
Wang, Y. F., Q. Cheng, and Q. Zhu. 2015. "Surface microscopic examination of quartz grains from rock avalanche basal facies." *Can. Geotech. J.* 52 (2): 167–181. https://doi.org/10.1139/cgj-2013-0284.
Wang, Y. F., J. J. Dong, and Q. G. Cheng. 2018. "Normal stress-dependent frictional weakening of large rock avalanche basal facies: Implications for the rock avalanche volume effect." *J. Geophys. Res.: Solid Earth* 123 (4): 3270–3282. https://doi.org/10.1002/2018JB015602.
Xu, C., X. Xu, J. B. H. Shyu, M. X. Gao, X. B. Tan, Y. K. Ran, and W. J. Zheng. 2015a. "Landslides triggered by the 20 April 2013 Lushan, China, Mw 6.6 earthquake from field investigations and preliminary analyses." *Landslides* 12 (2): 365–385. https://doi.org/10.1007/s10346-014-0546-1.
Xu, C., X. W. Xu, and J. B. H. Shyu. 2015b. "Database and spatial distribution of landslides triggered by the Lushan, China Mw 6.6 earthquake of 20 April 2013." *Geomorphology* 248: 77–92. https://doi.org/10.1016/j.geomorph.2015.07.002.
Yin, Y., F. Wang, and P. Sun. 2009. "Landslide hazards triggered by the 2008 Wenchuan earthquake, Sichuan, China." *Landslides* 6 (2): 139–152. https://doi.org/10.1007/s10346-009-0148-5.
Yuan, R. M., C. L. Tang, J. C. Hu, and X. W. Xu. 2014. "Mechanism of the Donghekou landslide triggered by the 2008 Wenchuan earthquake revealed by discrete element modeling." *Nat. Hazards Earth Syst. Sci.* 14 (5): 1195–1205. https://doi.org/10.5194/nhess-14-1195-2014.
Zhang, M., L. Wu, J. Zhang, and L. Li. 2019. "The 2009 Jiweishan rock avalanche, Wulong, China: deposit characteristics and implications for its fragmentation." *Landslides* 16: 893–906. https://doi.org/10.1007/s10346-019-01142-6.
Zhang, M., and Y. P. Yin. 2013. "Dynamics, mobility-controlling factors and transport mechanisms of rapid long-runout rock avalanches in China." *Eng. Geol.* 167: 37–58.
Zhang, M., Y. P. Yin, and M. McSaveney. 2016. "Dynamics of the 2008 earthquake-triggered Wenjiagou Creek rock avalanche, Qingping, Sichuan, China." *Eng. Geol.* 200: 75–87. https://doi.org/10.1016/j.enggeo.2015.12.008.
Zhang, N., and T. M. Evans. 2019. "Discrete numerical simulations of torpedo anchor installation in granular soils." *Comput. Geotech.* 108: 40–52. https://doi.org/10.1016/j.compgeo.2018.12.013.
Zhao, T., and G. B. Crosta. 2018. "On the dynamic fragmentation and lubrication of coseismic landslides." *J. Geophys. Res.: Solid Earth* 123 (11): 9914–9932. https://doi.org/10.1029/2018JB016378.
Zhao, T., G. B. Crosta, S. Utili, and F. V. De Blasio. 2017. "Investigation of rock fragmentation during rockfalls and rock avalanches via 3-D discrete element analyses." *J. Geophys. Res.: Earth Surface* 122 (3): 678–695. https://doi.org/10.1002/2016JF004060.
Zhou, G. G., and Q. C. Sun. 2013. "Three-dimensional numerical study on flow regimes of dry granular flows by DEM." *Powder Technol.* 239: 115–127. https://doi.org/10.1016/j.powtec.2013.01.057.
Zhou, J. W., P. Cui, and X. G. Yang. 2013. "Dynamic process analysis for the initiation and movement of the Donghekou landslide-debris flow triggered by the Wenchuan earthquake." *J. Asian Earth Sci.* 76: 70–84. https://doi.org/10.1016/j.jseaes.2013.08.007.
Zhou, W., Z. Lai, G. Ma, L. Yang, and Y. Chen. 2016. "Effect of base roughness on size segregation in dry granular flows." *Granular Matter* 18 (4): 83. https://doi.org/10.1007/s10035-016-0680-7.
Zou, Z. X., H. M. Tang, C. R. Xiong, A. J. Su, and E. R. Criss. 2017. "Kinetic characteristics of debris flows as exemplified by field investigations and discrete element simulation of the catastrophic Jiweishan rockslide, China." *Geomorphology* 295: 1–15. https://doi.org/10.1016/j.geomorph.2017.06.012.